AFRL-AFOSR-VA-TR-2019-0066

New Generation Optical Nanotransformers for NIR-to-Visible Image Up-conversion and Friend-Foe Identification

Paras Prasad
RESEARCH FOUNDATION OF STATE UNIVERSITY OF NEW YORK THE
402 CROFTS HALL
BUFFALO, NY 142600001

03/15/2019
Final Report

Air Force Research Laboratory
AF Office Of Scientific Research (AFOSR)/RTB2

Arlington, Virginia 22203
Air Force Materiel Command

REPORT DOCUMENTATION PAGE

Form Approved
OMB No. 0704-0188

1. REPORT DATE *(DD-MM-YYYY)*	2. REPORT TYPE	3. DATES COVERED *(From - To)*
15-03-2019	Final Performance	15 Sep 2015 to 14 Sep 2018

4. TITLE AND SUBTITLE
New Generation Optical Nanotransformers for NIR-to-Visible Image Up-conversion and Friend-Foe Identification

5a. CONTRACT NUMBER

5b. GRANT NUMBER
FA9550-15-1-0358

5c. PROGRAM ELEMENT NUMBER
61102F

6. AUTHOR(S)
Paras Prasad

5d. PROJECT NUMBER

5e. TASK NUMBER

5f. WORK UNIT NUMBER

7. PERFORMING ORGANIZATION NAME(S) AND ADDRESS(ES)
RESEARCH FOUNDATION OF STATE UNIVERSITY OF NEW YORK THE
402 CROFTS HALL
BUFFALO, NY 142600001 US

8. PERFORMING ORGANIZATION REPORT NUMBER

9. SPONSORING/MONITORING AGENCY NAME(S) AND ADDRESS(ES)
AF Office of Scientific Research
875 N. Randolph St. Room 3112
Arlington, VA 22203

10. SPONSOR/MONITOR'S ACRONYM(S)
AFRL/AFOSR RTB2

11. SPONSOR/MONITOR'S REPORT NUMBER(S)
AFRL-AFOSR-VA-TR-2019-0066

12. DISTRIBUTION/AVAILABILITY STATEMENT
A DISTRIBUTION UNLIMITED: PB Public Release

13. SUPPLEMENTARY NOTES

14. ABSTRACT
In this project, we explored new generation photon conversion nanomaterials that can harvest light over a broad spectral range and subsequently convert it with a spectral shift. We have developed new pathways involving energy harvesting by a strong dye absorber and subsequent energy transfer to a lanthanide ions in the nanocrystals. The introduction of this new pathway allowed us to address the fundamental limit of the weak and narrow IR absorption of rare-earth upconverters, as long as the concentration quenching of rare earth elements themselves. This type of lanthanide doped materials holds the great potential because they can tolerate harsh environments and easily scale up to produce.

15. SUBJECT TERMS
upconversion nanocomposites, excited state engineering, hybrid organic inorganic nanoparticles

16. SECURITY CLASSIFICATION OF:			17. LIMITATION OF ABSTRACT	18. NUMBER OF PAGES	19a. NAME OF RESPONSIBLE PERSON
a. REPORT	b. ABSTRACT	c. THIS PAGE			CASTER, KENNETH
Unclassified	Unclassified	Unclassified	UU		19b. TELEPHONE NUMBER *(Include area code)* 703-588-8487

Standard Form 298 (Rev. 8/98)
Prescribed by ANSI Std. Z39.18

Final Report

Contract/Grant Title: New Energy Transfer Pathways in Optical Nanotransformers for NIR-to-Visible Image Upconversion and Friend-Foe Identification

Contract/Grant#: Grant No. FA9550-15-1-0358

Reporting Period: 09/15 to 09/18

The main goal of this project was to explore new generation, highly efficient photon conversion nanomaterials, using new energy transfer pathways for harvesting of light over a broad spectral range and subsequent efficient spectrally shifted conversion. We have developed such new pathways involving energy harvesting by a strong dye absorber and subsequent energy transfer to a lanthanide ions in the fluoride nanocrystals (nanophosphors). Specifically: We have prepared efficient broadband upconversion organic dye-sensitized core/active shell nanocrystals to upconvert near infrared light; We devised a way to alleviate the luminescence concentration quenching of upconversion nanoparticles via sensitization by ICG dye of various concentrations; We greatly improved quantum cutting by sensitization of downconverting nanparticles with aggregation enhanced emission dyes; Using our innovative optical nanotransformers we successfully demonstrated subcellular optogenetic neuro-modulation with upconverted near infrared light; We also demonstrated tunable narrow band emission in the second near infrared biological window using dye-sensitized core/shell/shell nanocrystals; We developed core–multiple shell nanostructures enabling concurrent upconversion and quantum cutting for photon management; Finally, we demonstrated the use of our organic dye sensitized upconverting nanophosphors for theranostics applications via simultaneous imaging and local heating.

A.1.Efficient broadband upconversion of near infrared light covering a wide infrared region

Upconversion (UC) nanoparticles have distinct advantages over other luminescent materials, such as spectrally distinct and narrow emission, non-blinking, and unique photo-stability. However, the weak and narrow-band NIR absorption of UCNPs remains intact, which caps their photon harvesting capability, and thus suppresses the UC luminescence output substantively. For example, the sensitizer ion Yb^{3+} absorbs light in narrow spectral window of ~1026-10660 cm^{-1} (~10 times narrower than that of an organic dye), and with a critically small absorption cross-section of ~10^{-17}-10^{-16} cm^2). Employing organic dyes as antennae on the UC nanoparticles can be an efficient strategy. In this study, we propose a new design of multidimensional energy cascaded upconversion in a series of the hybrid organic–inorganic nanosystems consisting of an epitaxial core/active shell upconverting nanocrystal with the organic NIR dye molecules anchored on to the nanocrystal surface (Figure A.1.1), which is shown to enable broadband upconversion of NIR light into a range of visible multicolor emissions with efficiency reaching ≈16.4% (UCL quantum yield of ≈9.2%). The NIR dyes are

designated to broadly and strongly harvest NIR light, with subsequent nonradiative energy transfer to lanthanide sensitizers of two types in the shell, and then to the lanthanide ions positioned within the inorganic core to entail an efficient upconversion process (Figure A.1.1a). The singlet state of the NIR dye is solely involved in the processes of light harvesting and energy transfer, which precludes the detrimental effect (the quenching of the triplet state) by oxygen molecules in environment. Importantly, simultaneous incorporation of distinct types of lanthanide ions in the shell layer enables a plethora of multi-dimensional pathways for a synergistically enhanced transport of the excitation energy from the NIR dyes on the surface of the core/active shell nanocrystal to the Yb^{3+} ions (the sensitizer) in the core nanocrystal (multidimensional energy transfer with calculated efficiency up to 98%). Since a set of X^{3+} (X = Er, Ho, Tm) activators have been incorporated into the inorganic core, the multiple paths of energy transfer fuel a palette of upconverted multicolor output through well-established energy transfers from the sensitizer Yb^{3+} to the activator X^{3+}.

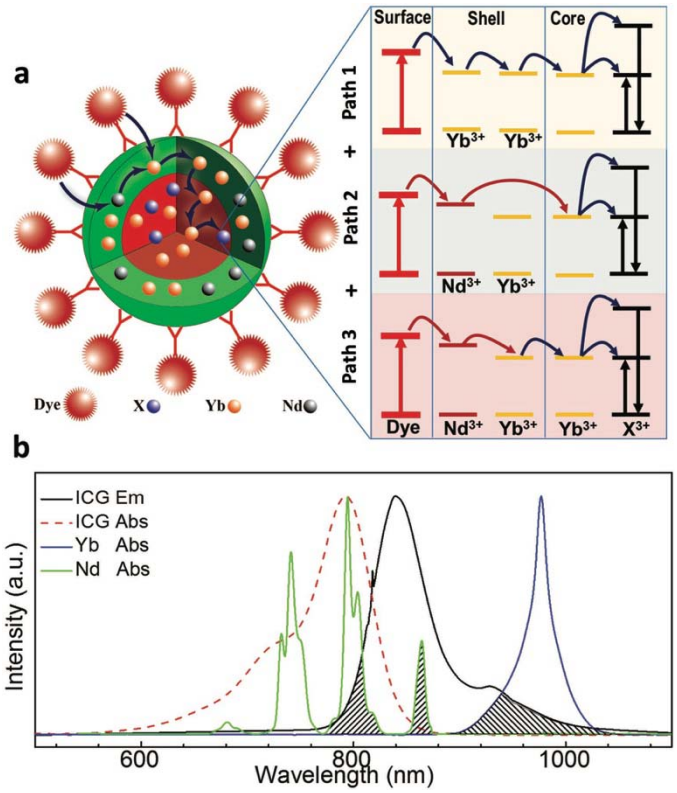

Figure A.1.1. Multidimensional energy cascaded upconversion in dye-sensitized core/active shell nanocrystals. a) Schematic illustration of multidimensional energy transfer pathways from the NIR dye molecules on the surface of the core/active shell nanocrystal of ($NaYF_4$:Yb^{3+}/X^{3+})@$NaYF_4$:Nd^{3+}/ Yb^{3+} to the lanthanide ions in the core. b) Absorption (red dashed line) and emission (black solid line) spectra of ICG dye versus the absorption spectra of Nd^{3}+ (solid green line) ions and Yb^{3+} (solid blue line)

To design the core/active shell nanocrystal, we utilize the hexagonal phase $NaYF_4$ host lattice with low phonon energy (<350 cm−1), which has been s hown to be one of the most efficient host materials to produce UCL, with minimized nonradiative losses at the intermediate electronic states of lanthanide ions. Two types of lanthanide ions, Nd^{3+} and Yb^{3+}, have been simultaneously incorporated into the active shell at precisely defined concentrations to allow for a multiple pathway for an efficient cascading of the excitation energy from the indocyanine green (ICG) dye on the core/shell nanocrsytal surface to the Yb^{3+}/X^{3+} (X = Er, Ho, Tm) ion pairs in the inorganic core (Figure A.1.1a). The NIR ICG dye is used in this work, because it possesses good stability and luminescence quantum yield and has been in wide usage. Moreover, a strong overlap of the emission spectrum of the ICG dye (750−1000 nm) with the absorption peaks of Nd^{3+} (peaked at ≈800 and 850 nm) as well as the absorption peak of Yb^{3+}

(peaked at≈976nm), allows for Forster-type energy transfer from the excited ICG molecules (energy donor) to both Nd^{3+} and Yb^{3+} acceptors in the shell layer (Figure A.1.1b). The energy cascading from the ICG dye on the core/shell nanocrystal surface to the sensitizer Yb^{3+} ion in the core involves three main paths (Figure A.1.1a): (1) The excited energy is transferred from ICG across the organic/inorganic interface to Yb^{3+} incorporated in the shell layer, and subsequently migrates through the Yb^{3+} shell sub-lattice to the Yb^{3+} ions in the core. (2) The harvested energy is transferred from the dye across the organic/inorganic interface to the Nd^{3+} ions in the shell, which then sensitize the Yb^{3+} ions in the core. (3) The harvested energy is transferred from ICG to the Nd^{3+} ions in the shell layer and then, unlike in Path 2, is transferred otheYb^{3+}ions also in the shell. It then migrates through the Yb^{3+} sub-lattice in the shell to the Yb^{3+} ions in the core. The synergy of the three paths provides highly effective transfer of the harvested energy from the NIR absorbing dye on the surface to the upconverting ions in the core of the nanocrystal, thus empowering efficient broadband upconversion of NIR light.

To demonstrate the principle of multidimensional energy transfer, we first validated the Yb^{3+}-induced energy transfer pathway (path 1) for dye-sensitized upconversion in the core/active shell nanocrystals of ($NaYF_4$:20%Yb^{3+}/X^{3+})@$NaYF_4$:20%Yb^{3+}, and then combined it with Nd3+-induced dual paths to exploit the synergistic effect on the UCL from the dye-sensitized core/active shell nanocrystals of ($NaYF_4$:20%Yb^{3+}/X^{3+})@$NaYF_4$: 20%Yb^{3+}, 30% Nd^{3+} (Path 2 and Path 3). The core/active shell nanocrystals of ($NaYF_4$:20%Yb^{3+}/X^{3+})/ $NaYF_4$:20%Yb^{3+} were prepared using a synthetic protocol adapted from literature. Transmission electron microscopy (TEM) images indicate that the synthesized core/active shell nanocrystals of ($NaYF_4$:20%Yb^{3+}/X^{3+})@$NaYF_4$: 20%Yb^{3+} (X = Er, Tm, and Ho) are spherical and monodispersed, with a mean size of ≈ 33 nm (Figure A.1.2b). The mean size of ≈ 26 nm for the core nanocrystals with a uniform spherical shape suggests a shell thickness of ≈ 3.5 nm for the core/active shell nanocrystals (Figure A.1.2a). Moreover, both

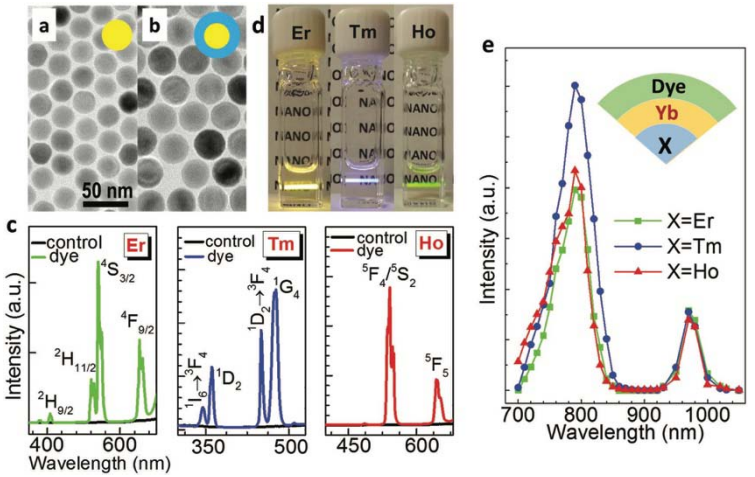

Figure A.1.2. The core/active shell nanocrystals of (NaYF4:Yb^{3+}/X^{3+})/$NaYF_4$:Yb^{3+} (X = Er, Tm, and Ho) sensitized by the ICG dye. TEM image of the synthesized a) $NaYF_4$:Yb^{3+} 20%, Er^{3+}2% core nanocrystals and b) ($NaYF_4$:Yb^{3+} 20%, Er^{3+} 2%)@$NaYF_4$: Yb^{3+} 20% core/active shell nanocrystals. c) UCL spectra of the ICG-sensitized (NaYF4:Yb^{3+} 20%, Er^{3+} 2%)@$NaYF_4$:Yb^{3+} 20%, (NaYF4:Yb^{3+} 20%, Tm^{3+} 0.5%)@$NaYF_4$:Yb^{3+} 20%, ($NaYF_4$:Yb^{3+} 20%, Ho^{3+} 2%)@$NaYF_4$:Yb^{3+} 20% core/shell nanocrystals, and of the corresponding control samples (without ICG). d) Photographic images of UCL from ICG-sensitized ($NaYF_4$:Yb^{3+} 20%, X^{3+})@$NaYF_4$:Yb^{3+} 20% (X = Er, Tm, and Ho) core/shell nanocrystals dispersed in DMF. e) The normalized UCL excitation spectra for ICG dye-sensitized ($NaYF_4$:Yb^{3+} 20%, X^{3+})@$NaYF_4$:Yb^{3+} 20% (X = Er, Tm, and Ho) core/shell nanocrystals dispersed in DMF.

the synthesized core and the core/active shell nanocrystals have been confirmed to be of hexagonal crystallographic phase. When compared with commonly investigated ($NaYF_4$:20%Yb^{3+}/X^{3+})@$NaYF_4$ core/inert nanocrystals, the core/active shell nanocrystals of ($NaYF_4$:20%Yb^{3+}/X^{3+})@ $NaYF_4$:20%Yb^{3+} (X = Er, Tm, and Ho) not only spatially isolate the core from the environment to sup- press surface-related luminescence quenching of the core but also provide an extra amount of sensitizer Yb^{3+} ions to enhance light harvesting within the absorption range (≈920−1050 nm) of Yb^{3+} ions and the processes of energy transfer from the sensitizer Yb^{3+} to the activators X^{3+} (X = Er, Tm, and Ho). As a result, direct excitation of Yb3+ ions enables the core/active shell (containing Yb^{3+} in the shell) to produce stronger UCL than the core/inert shell (without Yb^{3+} in the shell) when excited at ≈980 nm. The UCL intensity from the core/active shell nanocrystals of ($NaYF_4$:20%Yb^{3+}/X^{3+})/$NaYF_4$:20%Yb^{3+} (X = Er, Tm, and Ho) is about 3–4 times higher than that from the corresponding core/inert nanocrystals of ($NaYF_4$:20%Yb^{3+}/X^{3+})/$NaYF_4$ (X = Er, Tm, and Ho) (for the same nanocrystal concentrations). Importantly, the incorporation of Yb^{3+} into the shell also provides shell-mediated sensitization of the core nanocrystal by the dye in a core/shell/dye structure.

To investigate the effect of ICG sensitization on the core/active shell nanocrystals of ($NaYF_4$:20%Yb^{3+}/X^{3+})/$NaYF_4$:20%Yb^{3+}, the long-chain ligand of oleic acid ($C_{18}H_{34}O_2$), originally capped on the nanocrystal surface, was first replaced by a short ionic ligand ($NOBF_4^-$) using a protocol adapted from literature to allow a close contact between the ICG dye and the core/shell nanocrystal. When introducing the ICG dye into surface-treated core/active shell nanoparticle dispersions in dimethylformamide (DMF) and irradiating them with laser at ≈800nm (far beyond the absorption range of Yb^{3+}), bright yellow, blue, and green UCL can be seen for the core/active shell nanocrystals of ($NaYF_4$:20%Yb^{3+}/2%Er^{3+})@ $NaYF_4$:20%Yb^{3+}, ($NaYF_4$:20%Yb^{3+}/0.5%Tm^{3+})@$NaYF_4$:20%Yb^{3+}, and ($NaYF_4$:20%Yb^{3+}/2%Ho^{3+})@$NaYF_4$:20%Yb^{3+}, correspondingly (Figure A.1.2d). The dependency of the integrated UCL intensity of (NaYF4:20%Yb^{3+}/X^{3+})@$NaYF_4$:20%Yb^{3+} (X = Er, Tm, and Ho) nanocrystals on the ICG dye concentration has been investigated. The optimum concentration was determined to be 75, 37, and 27 μg mL^{-1} for the core/ active shell nanocrystals with activators of Er^{3+}, Tm^{3+}, and Ho^3+, respectively. Furthermore, the UCL from ICG dye-sensitized ($NaYF_4$:20%Yb^{3+}/X^{3+})@$NaYF_4$:20%Yb^{3+} (X = Er, Tm, and Ho) nanocrystals with optimized dye concentrations is ≈3000 times stronger than that from the corresponding control samples without ICG (Figure A.1.2c). The broad and intense band peaked at ≈800 nm in the UCL excitation spectra for the dye-sensitized core/ active shell nanocrystals corresponds to the absorption band of the ICG dye in Figure A.1.2e. Taken together, these results indicate the successful sensitization of the Yb^{3+} ions in the shell of the nanocrystals of ($NaYF_4$:20%Yb^{3+}/X^{3+})@$NaYF_4$:20%Yb^{3+} (X = Er, Tm, and Ho), which will elicit energy migration through Yb3+ sub-lattice to the Yb^{3+} ions in the core, yielding UCL through well-established processes of energy transfer upconversion. Moreover, the excitation spectra also shows that ICG-sensitized ($NaYF_4$:20%Yb^{3+}/X^{3+})@$NaYF_4$:20%Yb^{3+} (X = Er, Tm, and Ho) nanocrystals can be ≈3−4 times more efficient when excited at ≈800 nm than at ≈980 nm. We evaluated the upconversion efficiencies for ICG-sensitized ($NaYF_4$:20%Yb^{3+}/X^{3+})@$NaYF_4$:20%Yb^{3+} (X = Er, Tm, and Ho) to be ≈ 7%–9% (UCL

quantum yield of ≈4%–5%) under the 800 nm excitation with power density of ≈8 W cm^{-2}. We then compared three types of ICG-sensitized core/active shell nanocrystals of ($NaYF_4$:Yb^{3+}/X^{3+})@$NaYF_4$:Yb^{3+} (energy transfer path 1 is involved), ($NaYF_4$:Yb^{3+}/X^{3+})@$NaYF_4$:Nd^{3+} (path 2 is involved), and ($NaYF_4$:Yb^{3+}/X^{3+})@$NaYF_4$:Nd^{3+}/Yb^{3+} (paths 1, 2, and 3 are involved) (X = Er, Tm, and Ho) (Figure A.1.3a). These core/active shell nanocrystals contained almost the same concentrations of Yb^{3+} and Nd^{3+}, as confirmed by the absorption spectra. All these nanocrystals are of hexagonal crystallographic phase and have almost identical core size and shell thickness as shown in Figure A.1.2a. The UCL spectra obtained from all these dye-sensitized core/ active shell nanocrystals are similar to the corresponding ones in Figure A.1.2c. The UCL intensity of ICG-sensitized ($NaYF_4$:Yb^{3+}/ X^{3+})@$NaYF_4$:Nd^{3+} nanocrystals is typically higher than that of ICG-sensitized ($NaYF_4$:Yb^{3+}/X^{3+})@$NaYF_4$:Yb^{3+} nanocrystals at the same dye concentration, while ICG-sensitized core/active shell nanocrystals of ($NaYF_4$:Yb^{3+}/X^{3+})@$NaYF_4$:Nd^{3+}/ Yb^{3+} (X = Er, Ho, and Tm) display the most intensive UCL, due to a synergistic effect from the multidimensional energy transfer (Figure A.1.3a). The excitation spectra indicate that the difference in the UCL intensity for these three types of core/shell nanostructures originates from the different degree of sensitization by the ICG dye (Figure A.1.3b). To confirm this, the fluorescence lifetime of the ICG dye was measured and evaluated to be ≈ 1.73, 0.92, 0.35, and 0.23 ns for the free dye, ICG-sensitized ($NaYF_4$:Yb^{3+} 20%, Er^{3+}2%)@$NaYF_4$:Yb^{3+} 20% nanocrystals, ICG-sensitized ($NaYF_4$:Yb^{3+} 20%, Er^{3+}2%)@$NaYF_4$:Nd^{3+} 20% nanocrystals, and ICG-sensitized ($NaYF_4$:Yb^{3+} 20%, Er^{3+}2%)@ $NaYF_4$:Nd^{3+} 30%, Yb^{3+} 20% nanocrystals, dispersed in DMF (Figure A.1.3d). Using the equation ET = 1 $-\tau_{DA}/\tau_D$, where ET is energy transfer efficiency and τ_{DA} and τ_D are the effective life- times of the energy donor in the absence and the presence of an energy acceptor, it can be determined that the measured lifetimes correspond to an efficiency of ≈47%, ≈ 80%, and 87%, for energy transfer between the ICG dye on the nanocrystal surface and the Yb^{3+}, Nd^{3+}, and Nd^{3+}/Yb^{3+} ions, respectively.

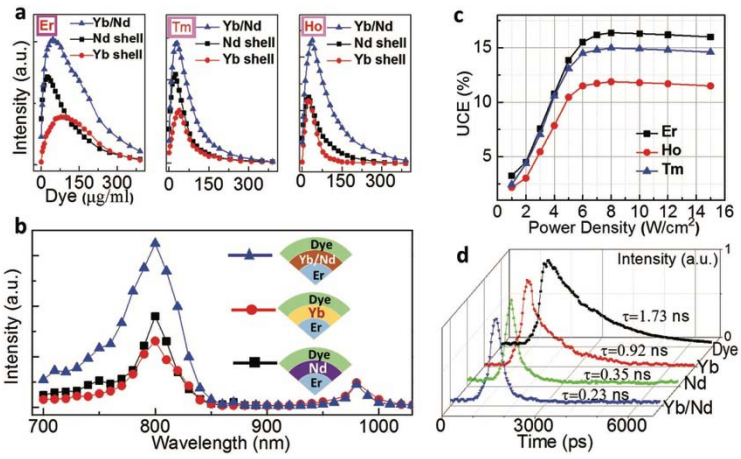

Figure A.1.3. Comparison of three types of core/active shell nanocrystals. a) Dependence of the integrated emission intensities from the $^4S_{3/2}$ state of Er^{3+}, from the $^1G_4$ state of Tm^{3+}, and from the $^5F_4/5S_2$ state of Ho^{3+} from ICG-sensitized core/active shell nanocrystals of ($NaYF_4$:Yb^{3+}/ X^{3+})@$NaYF_4$:Yb^{3+}, ($NaYF_4$:Yb^{3+}/X^{3+})@$NaYF_4$:Nd^{3+}, and ($NaYF_4$:Yb^{3+}/X^{3+})@$NaYF_4$:Nd^{3+}/Yb^{3+} (X = Er, Tm, and Ho), on the concentration of the ICG dye. b) UCL excitation spectra (for the integrated emission intensities from the $^4S_{3/2}$ state of Er^{3+}) for ICG dye-sensitized core/active shell nanocrystals. c) Dependence of the estimated upconversion efficiencies (UCE) for core/active shell nanocrystals on the excitation power density. d) Fluorescence decays of free ICG in DMF (black), and ICG on the surface of the core/active shell

Note that the lifetime values extracted from green and blue curves in Figure A.1.3d are quite close to the instrument response to the exciting laser pulse of ≈0.18 ns, meaning that the measured values of 0.35 and 0.23 ns actually determine the upper limits of the corresponding real values. As a result, the real ET efficiencies are at least ≈80% and 87% from the ICG dye to the Nd^{3+} ions or Nd^{3+}/Yb^{3+} ions in the shell, respectively. Moreover, we have employed theoretical modeling to investigate the overall efficiencies of energy transfer via three pathways: 1) Dye → Yb in the shell → Yb in core (path 1); 2) Dye → Nd in the shell → Yb in core (path 2); 3) Dye → Nd/Yb in the shell → Yb in core (path 1+ path 2+ path 3). The overall efficiencies were calculated to be 40%, 58%, and ≈98% for scheme 1, scheme 2, and scheme 3, respectively, confirming that the most efficient sensitization process occurs for the $(NaYF_4:Yb^{3+}/X^{3+})@NaYF_4:Nd^{3+}/Yb^{3+}$ (X = Er, Tm, and Ho) core/active shell nanocrystals sensitized by the NIR dye. Indeed, the upconversion efficiencies of the ICG-sensitized core/active shell nanocrystals of $(NaYF_4:Yb^{3+}/X^{3+})@NaYF_4:Nd^{3+}/Yb^{3+}$ were determined to be as high as ≈16.4%, 14.9%, and 11.8% (upconversion quantum yield of ≈9.2%, 7.7%, and 7.3) for activators of X = Er, X = Tm, and X = Ho, respectively, under ≈800 nm excitation (8 W cm^{-2}).

We found that the photostability of the dye sensitization system described in Figure A.1.3 is similar to that of pure ICG dyes in DMF, Tm, and Ho) organic–inorganic composite is stable, as the dye sensitization effect remains efficient even with laser irradiation at 800 nm of 8 W cm^{-2} for up to 5 h. It is worth noting that the design of the dye-UC nanoparticle system also provides additional possibilities to switch and tune UC. For example, use of other dyes with absorption/emission at longer wavelengths would allow to directly employ Yb^{3+} ions as efficient energy acceptor, without intermediate Nd^{3+} ions. Similarly, with further shift of dye absorption/emission toward NIR (e.g., beyond 1 μm), a possibility will open to employ other ions as energy acceptors/sensitizers. On the other hand, by reducing the size of the core–shell nanoparticles, one can increase the part of the sensitizer ions that is directly reachable by energy transfer from the dye molecules, which might also increase the energy transfer efficacy. Such a flexibility of the proposed energy- transfer-based upconversion nanoplatform would be beneficial for development of nanomaterials capable of upconversion in different infrared regions.

We have demonstrated the potential of our highly efficient ICG-sensitized core/active shell nanocrystals for two applications. First, a proof-of-concept experiment showing perspectives of multicolor display application was implemented (Figure A.1.4). The ICG-sensitized $(NaYF_4:Yb^{3+}/X^{3+})@NaYF_4:Nd^{3+}/ Yb^{3+}$ (X = Er, Tm, and Ho) were doped with a defined weight ratio of ≈1 wt% into the polydimethylsiloxane (PDMS) cylinders (radius = 1.3 cm, height = 1.4 cm). The black letters printed on a plain white paper can be perceived with crystal clearness through a 1.4 cm thick PDMS of the resulted cylinders, demonstrating the transparent quality of these nanocrystals-doped PDMS cylinders. When excited at 800 nm, these PDMS cylinders are able to emit bright UCL with a range of colors visible under regular lighting conditions (Figure A.1.4a). Moreover, multicolored UCL patterns (Figure A.1.4b) can be visualized through an input of the framed laser beam at a defined low power excitation density (0.1 W cm^{-2}), suggesting uses of the composite of PDMS and ICG-sensitized core/active shell

nanocrystals for volumetric multicolor displays. In a second demonstration, the potential application of ICG-sensitized core/active shell nanocrystals for optical (UCL) bioimaging was illustrated. An amphiphilic polymer DSPE-mPEG-2000 (1,2-distearoyl-sn-glycero-3-phosphoethanolamine-N-methoxy(polyethylene glycol)-2000) was utilized to encapsulate dye-sensitized nanoparticles within micelles, rendering them dispersible in an aqueous phase.It was found that the intensity of UCL from ICG-sensitized ($NaYF_4$:Yb^{3+}/Er^{3+})@$NaYF_4$:Nd^{3+}/Yb^{3+} core/active shell nanocrytals decreased ≈5 times after the phase transfer from DMF to water. However, the remaining UCL intensity is still adequate to be visualized and utilized for cellular imaging. In addition, multi-colored UCL from ICG-sensitized core/active shell nanocrystals encapsulated within phospholipid micelles in aqueous phase holds promise for potential use in multiplexed bioimaging.

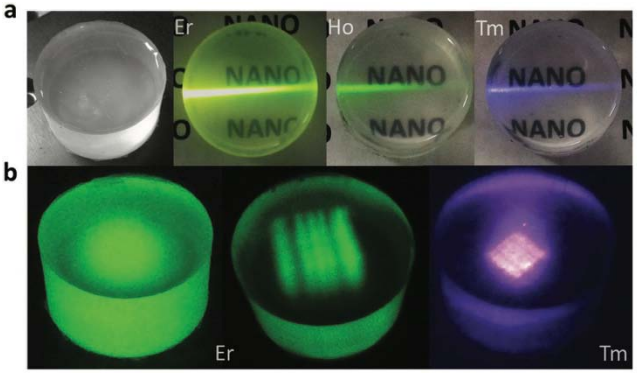

Figure A.1.4. Potential application of core/active shell nanocrystals sensitized by ICG dye for multicolor displays.

A.2. Alleviation of luminescence concentration quenching of upconversion

One major obstacle for the application of UC nano-materials is the concentration quenching effect at high doping levels of the activator, which sets a limit on the amount of lanthanide emitters. Typically, the doping concentration of activators is confined below 2 mol% to avoid the concentration quenching effect. we introduced a simple and reliable approach to break the concentration quenching threshold and significantly boost the UCL of UCNPs through near-infrared (NIR) dye sensitization. We selected indocyanine green (ICG) as the NIR dye and colloidal upconverting $NaYF_4$:Nd as a model system. The ICG dye was selected because it possesses a large absorption cross section (~6 × 10−16 cm^2), ~30 000 times higher than that of Nd^{3+} ions (~2 × 10−20 cm^2) at 800 nm, and its emission band strongly overlaps with the absorption peaks of the Nd^{3+} ions, enabling efficient non-radiative energy transfer from ICG to surface Nd^{3+} ions (Scheme A.2.1). The nanoparticles doped with Nd^{3+} alone are utilized because of the involved simple upconverting mechanism. We show that the optimal doping

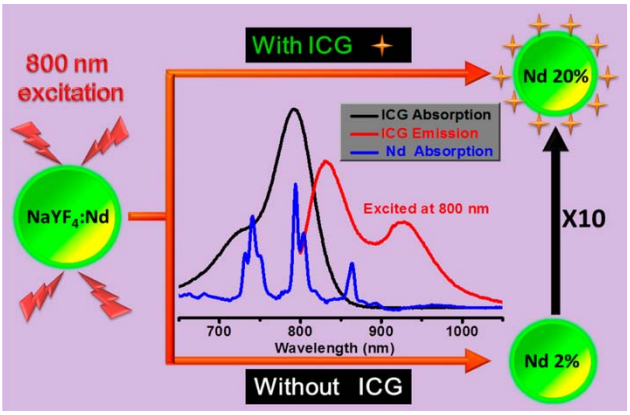

Scheme A.2.1. A brief description of the optimal Nd3+ doping concentration with and without ICG sensitization, and the realization of enhanced UCL with the presence of ICG, with the absorption spectrum of Nd^{3+} and the absorption and emission spectra of ICG shown in the center.

concentration of Nd^{3+} was shifted from 2 to 20 mol%, along with a 10-fold UCL enhancement through ICG dye sensitization.

A series of $NaYF_4$:Nd UCNPs with increasing Nd^{3+} were fabricated utilizing a method adapted from the literature. TEM images (Figure A.2.2a) show that all nanoparticles are uniform, with an average size of 18.2 ± 1.1 nm. The XRD results indicate that all samples are of hexagonal crystallographic phase (JCPDS No. 16-0334), favorable for high upconversion efficiency. Their UCL spectra are shown in Figure A.2.2b. The optimal doping concentration for Nd^{3+} turned out to be around 2 mol% (inset of Figure A.2.2b), similar to the optimized amount of other activators, Er^{3+}, Tm^{3+}, and Ho^{3+}, reported in the literature on UCNPs. The quenching of UCL beyond this critical concentration is ascribed to the well-known concentration quenching effect existing in a majority of lanthanide ions. From Figure A.2.2c, highly visible UCL can be observed from the $NaYF_4$:Nd UCNPs under 800 nm laser excitation. Interestingly, the emission color changed from green to orange with the elevated concentration of Nd^{3+}, in accordance with the spectral change in Figure A.2.2b. This is presumably due to the cross relaxation process [$^4F_{3/2} \rightarrow {}^4I_{9/2}$:$^4I_{15/2} \rightarrow {}^2G_{7/2}/{}^4G_{5/2}$] between two Nd^{3+} ions, resulting in the population increase of the yellow-emitting $^2G_{7/2}$ and $^4G_{5/2}$ states. The proposed underlying upconversion mechanism is shown in Figure A.2.2d. Upon 800 nm excitation, the Nd^{3+} ions in the ground state $^4I_{9/2}$ are first excited to the $^4F_{5/2}/{}^2H_{9/2}$ states. Some Nd^{3+} ions in these excited states rapidly relax to the $4F_{3/2}$ state through a multi-phonon-assisted process. The Nd^{3+} ions at the $^4F_{3/2}$ state are then promoted to higher excited states $^2D_{5/2}/{}^2P_{1/2}$ by absorbing a second photon or by energy transfer from a Nd^{3+} ion at the $^4F_{5/2}/{}^2H_{9/2}$ state. Subsequently, two-photon emissions centered at 413, 523, 588, 640, and 661 nm emerge, which are attributed to $^2D_{5/2}/{}^2P_{1/2} \rightarrow {}^4I_{9/2}$, $^4G_{7/2}/{}^2K_{13/2}/{}^4G_{9/2} \rightarrow {}^4I_{9/2}$, $^2G_{7/2}/G_{5/2} \rightarrow {}^4I_{9/2}$, $^2H_{11/2} \rightarrow {}^4I_{9/2}$, and $^4F_{9/2} \rightarrow {}^4I_{9/2}$ transitions, respectively. The dependence of the UCL intensities for distinct bands on the excitation power density was measured. The slopes of 523 and 588 nm UCL bands are determined to be 1.78 and 1.79, validating that the dominant emission bands originate from a two-photon process.

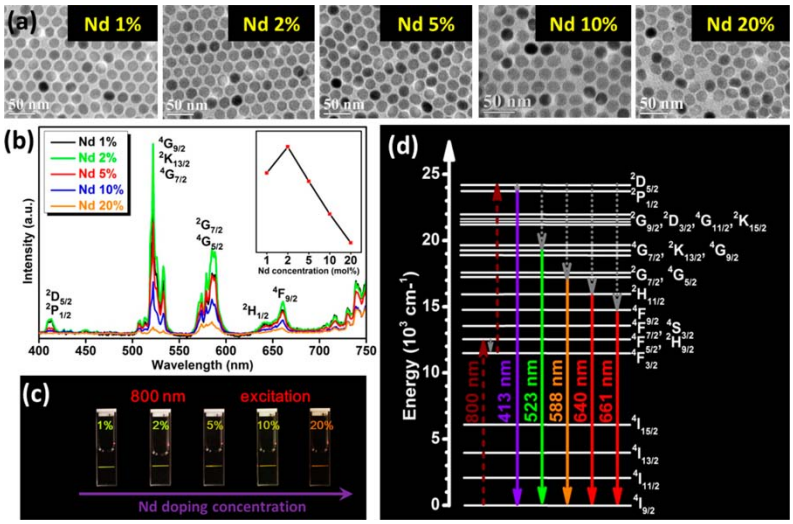

Figure A.2.2. (a) TEM images of $NaYF_4$:Nd UCNPs with different Nd doping levels. (b) UCL spectra of the as-synthesized $NaYF_4$:Nd UCNPs under 800 nm excitation at a power of 1 W. The UCNPs were dispersed in hexane with a concentration of 13 mg/mL. Inset: Integrated intensity of entire emission (400 to 700 nm) as a function of Nd^{3+} doping concentration. (c) Corresponding luminescence photographs of $NaYF_4$:Nd UCNPs under800 nm excitation at a power of 1 W (hexane dispersion, 1 wt%). (d) Proposed upconversion mechanism of Nd^{3+}-doped $NaYF_4$ UCNPs.

We next explored the optical behavior of a set of $NaYF_4$:Nd UCNPs (with different Nd^{3+} content) sensitized by ICG dye of various concentrations. To ensure a close contact between the UCNPs and ICG, the original oleic acid ligand capped on the as-synthesized nanoparticles was replaced by a short, ionic $NOBF_4$ ligand. Then the $NOBF_4$-coated UCNPs were dispersed in DMF for the following ICG sensitization experiment. Since 523 and 588 nm emissions are two dominant emissions in $NaYF_4$:Nd UCNPs (Figure A.2.2b), our following investigations are mainly focused on these two emissions and all the emission intensity refers to integrated intensity. According to FigureA.2.3a, the UCL intensities of all $NaYF_4$:Nd UCNPs were significantly

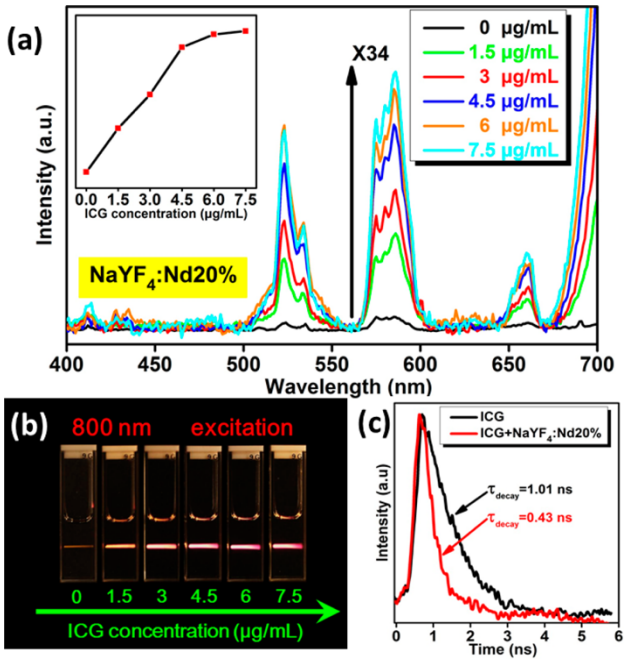

Figure A.2.3. (a) UCL spectra of $NaYF_4$:Nd20% with different ICG concentrations under 800 nm excitation. Inset: Integrated intensity of entire emissions (400 to 700 nm) as a function of the ICG concentration. (b) Corresponding UCL photographs of $NaYF_4$:Nd20% UCNPs with different ICGconcentrations. (c) Fluorescence lifetime curves of ICG with and without $NaYF_4$:Nd20% UCNPs.

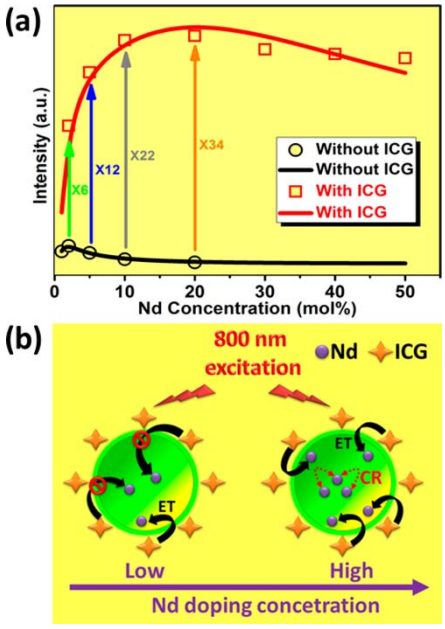

Figure A.2.4. (a) Experimental results (black circle and red square) and theoretical modeling (black and red curves) of integrated UCL intensities of a set of $NaYF_4$:Nd UCNPs with (6.0 μg/mL) and without ICG sensitization. (b) Schematic illustration of the energy transfer mechanism from ICG to $NaYF_4$:Nd UCNPs, considering both low and high Nd3+ doping levels with ICG sensitization.

improved with an increase amount of the ICG dye in solution, reaching a maximum at an ICG concentration of 6 μg/mL. Take the $NaYF_4$:Nd20% as an example (Figure A.2.3a), the UCL intensity increases about 34 times at the optimal ICG concentration, when compared with that of the $NaYF_4$:Nd20% UCNPs alone. Figure A.2.3b presents a clear UCL photograph of the increased brightness, providing the direct evidence of ICG sensitization under 800 nm excitation. We also measured the fluorescence decay curves of the ICG emission with and without the presence of $NaYF_4$:Nd20% UCNPs (Figure A.2.3c). As anticipated, the decay lifetime of the ICG dye was shortened from 1.01 to 0.43 ns due to the Forster-type non-radiative energy transfer from ICG to the surface Nd^{3+} ions. According to the equation ET = 1− τDA/τD, where ET is the energy transfer efficiency and τDA and τD are the effective lifetimes of the energy donor in the absence and the presence of an energy acceptor, the efficiency for

energy transfer from the ICG dye to the surface Nd^{3+} ions was estimated to be ~57%.

We then investigated the integrated UCL intensities of two dominant emissions at 523 and 588 nm from the $NaYF_4$:Nd UCNPs with and without ICG sensitization, as a function of Nd^{3+} concentration. As can be seen from Figure A.2.4a, the sensitization effect of ICG becomes more obvious at a higher Nd^{3+} doping level. About 6-, 12-, 22- and 34-fold UCL intensity increases were observed for 2, 5, 10, and 20 mol% Nd^{3+}-doped $NaYF_4$ UCNPs at the presence of 6.0 μg/mL ICG. This is reasonable, because when Nd^{3+} doping level is low, the amount of surface Nd^{3+} ions (the ions on or close to the UCNPs' surface) is low, producing a limited ICG sensitization effect. As the Nd^{3+} concentration increases, the amount of surface Nd^{3+} ions increases accordingly, introducing more channels to perform the ICG sensitization for every single $NaYF_4$:Nd UCNP. In Figure A.2.3a, it should be noted that the optimal concentration for Nd^{3+} without the presence of ICG is 2 mol%, while it shifts to 20 mol% with the existence of ICG. This means that the luminescence concentration quenching effect, which occurs at a high doping level of the lanthanide ions owing to self-quenching (mostly, cross-relaxation-induced quenching process), was alleviated through the ICG dye sensitization. Along with the increment of Nd^{3+} concentration, the cross-relaxation process induced self-quenching becomes more pronounced to diminish UCL more, while on the other hand high Nd^{3+} doping concentration favors ICG sensitization, which enhances UCL intensity. Figure A.2.4b briefly depicts the aforementioned competing processes that results in alleviation of luminescence concentration quenching effect. We envisioned that the coupling of enhanced NIR light harvesting due to the ICG dye having a ~30 000 times larger absorption section than Nd^{3+}ions, the efficacious Forster-type energy transfer from the ICG dye to the surface Nd^{3+} ions (~57% efficiency), and subsequent efficient energy migration among the Nd^{3+} ions are able to activate the Nd^{3+} ions that can compete with the concentration- induced luminescence quenching rate. We developed a simple phenomenological model to interpret the kinetics of the sensitization behavior of ICG with the variation of Nd^{3+} doping concentration. In short, in estimating the emission intensity of the sensitized UCNPs, we assumed that sensitization could be accounted for the modified cross section of the one-photon excitation of Nd^{3+} ions, followed by either excited state absorption or energy transfer upconversion. The dimensionless prefactor that quantifies this modification depends on the number of ICG molecules anchored on the surface of UCNPs, the absorption cross section of ICG, and the rate of resonance energy transfer from ICG to the adjacent Nd^{3+} ions. The competing process - a combination of concentration dependent self-quenching and cross relaxation- was assumed to be a short-range bi-exponential interaction. The results of our modeling are in good agreement with the experimental observations (Figure A.2.4a).

In summary, we described a simple strategy to alleviate the luminescence concentration quenching that is ubiquitous in lanthanide-based luminescent materials. The optimal doping concentration of Nd^{3+} in colloidal $NaYF_4$:Nd UCNPs was shifted from 2 to 20 mol% through sensitization by anchoring an ICG dye on the nanocrystal surface, along with ~10 times upconverting brightness increase. The dye sensitization effect (with enhanced light harvesting) as well as efficient energy migration among the Nd^{3+} ions leads to the optimal concentration shift and brightness increase by competing with the self-quenching effect. Our results open

opportunities to realize a higher UCL intensity at higher activator doping concentration, improving the performance of UCNPs that are actively engaged in a number of photonic applications.

A.3. Dramatic improvement of quantum cutting by sensitization with aggregation enhanced emission dyes

We proposed and demonstrated the feasibility of dye-sensitization with AIEE LPs to drive efficient quantum-cutting(QC) emission from NPs co-doped with Tb^{3+} and Yb^{3+} ions. The AIEE LPs can fully cover the surface of NPs, while conventional LPs must be separated by at least their own FRET radius to limit concentration quenching. Thus, all acceptor ions within one FRET radius of the surface of the NPs can receive energy from dye molecules, but conventional LPs could sensitize only a fraction of the acceptor ions (Figure A.3.1a). We exploited this superior sensitization capability to design and implement a cascade energy-transfer quantum cutting process consisting of four steps: (i) UV absorption by AIEE LPs, (ii) FRET between excited AIEE LPs and Tb^{3+}ions, (iii) quantum cutting by energy transfer from one excitedTb^{3+} ion to two excited Yb^{3+} ions, and (iv) emission from excited Yb^{3+} ions (Figure A.3.1b,c). As shown in Figure A.3.1c, the well-matched spectral overlap between emission of our AIEELPs and absorption of Tb^{3+} ions ($^5D_4$) can facilitate the FRET process, while Tb^{3+} and Yb^{3+} ions are a well-known pair for quantum cutting because of their perfect energy matching ($^5D_4$state of Tb^{3+}: 2.53 eV; $^2F_{7/2}$ state of Yb^{3+}: 1.265 eV). The QC emission of Yb^{3+} at 1.265 eV is perfectly matched with the most-efficient wavelength of photocurrent generation by a silicon solar cell for further application as discussed below. This QC produces two lower-energy photons from one high energy photon, with a theoretical quantum efficiency exceeding 100%. As an example of the practical utility of AIEE sensitized QC, we demonstrated the improved photovoltaic efficiency of a crystalline silicon solar cell by conversion of one UV photon, at an energy far above the bandgap of silicon, intotwo NIR photons that match the silicon bandgap and are, thus, efficiently utilized.

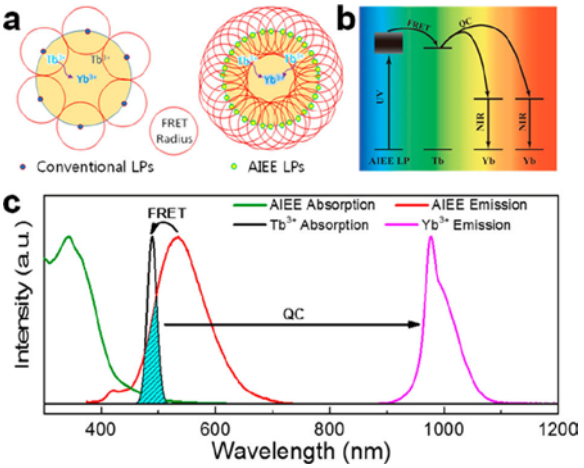

Figure A.3.1. Schemes of AIEE LP sensitized quantum cutting. (a) Schematic illustration of the difference between conventional and AIEE LPs in the sensitization of quantum cutting. (b) Energy-transfer pathway from the AIEE LPs to NaYF4:Yb^{3+},Tb^{3+} nanocrystals. (c) Absorption (green) and emission (red) spectra of the AIEE LP, absorption spectrum of Tb^{3+} (black), and emission spectrum of Yb^{3+} (pink). The dashed blue area highlights the overlap between the AIEELP emission and absorption of Tb^{3+}.

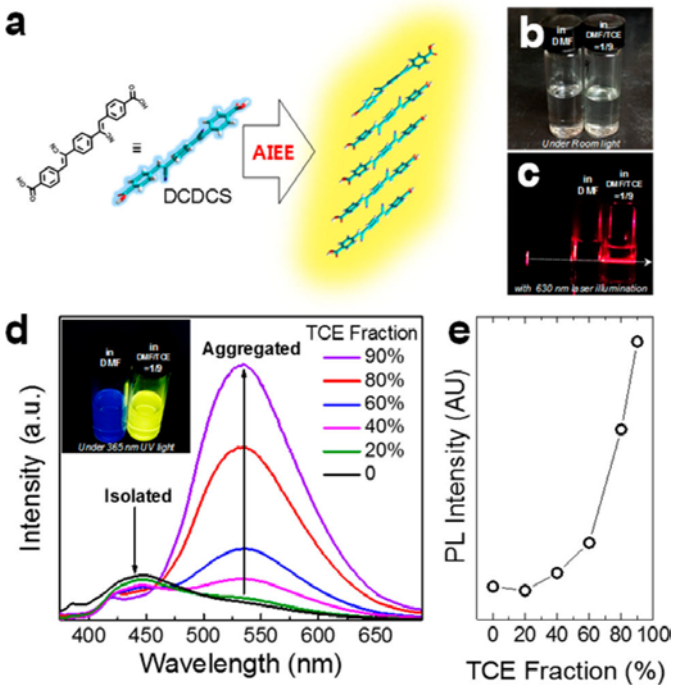

Figure A.3.2. AIEE behavior of DCDCS. (a) Schematic illustration of AIEE of DCDCS. Photographs under (b) room light and (c) 630 nm laser illumination of DCDCS in DMF and 90% TCE. The dotted white arrow in panel c shows the laser propagation direction. (d) Photoluminescence spectra of DCDCS in mixed solvents of varying TCE-to-DMF ratios. The inset is a photograph of DCDCS in DMF and in 90% TCE under 365 nm light illumination. (e) PL intensity of DCDCS as a function of TCE fraction in the solvent.

We designed and synthesized a new AIEE active dicyanostilbene derivative, 4,4-((1Z,1'Z)-1,4-phenylbis(2-cyanoethene-2,1-diyl)dibenzoic acid, DCDCS, that has two anchoring carboxylic acid groups for attachment to the surface of NPs (Figure A.3.2a). This type of dicyanostilbene (DCS) derivative has previously been of interest for its piezochromic AIEE emission property. Based on those reports, we examined the AIEE activity of DCDCS by inducing aggregation in a mixture of dimethylformamide (DMF, good solvent, polarity index of 6.4) and trichloroethylene (TCE, poor solvent, polarity index of 1.0). Because DCDCS exhibits some solubility in water (a typical poor solvent for AIEE LPs), we screened various less polar solvents and chose TCE to induce aggregation. DCDCS in 90% TCE showed clear Mie scattering under illumination by a 630 nm laser, while the solution in DMF showed no scattering (Figure A.3.2b,c). Accordingly, we measured photoluminescence spectra of DCDCS in TCE/DMF mixed solvents with varying TCE fractions. DCDCS aggregated with increasing TCE content, producing a bathochromic shift from 450 to 540 nm (Figure A.3.2d), as is typical of a cyanostilbene-based AIEE active luminophore. The dramatic growth of PL intensity with increasing poor solvent fraction is typical AIEE behavior (Figure A.3.2e). The fluorescence quantum yield of aggregated (in 90% TCE) DCDCS was enhanced to 47% from 13% for the solution in DMF.

Having established the AIEE behavior of DCDCS, we proceeded to test its ability to photosensitize quantum cutting in Yb^{3+}/Tb^{3+} co-doped NPs (QCNPs). We synthesized $NaYF_4$:50% Yb^{3+}, x% Tb^{3+} (x = 2, 5, 8, 12, 15) NPs by published methods. We varied the Tb^{3+} ion content because it is the direct acceptor of energy transfer from the AIEE dye. Transmission electron microscopy (TEM) images (Figures A.3.3a) showed average nanoparticle sizes of 34, 33, 32, 30,and 29 nm for Tb^{3+} doping levels of 2%, 5%, 8%, 12%, and 15%, respectively. A slight variation in the nanoparticle size is due to the ionic size of Tb^{3+} (0.923 Å) being larger than Y^{3+} (0.9 Å). X-ray diffraction showed that all NPs were in the expected hexagonal phase. Under 405 nm laser excitation, the emission intensities of 4 mg of each nanoparticle sample were almost negligible (Tb^{3+} and $^5D_3$). Among them,8% Tb^{3+} doped

NPs showed stronger emission than the others. We then added 100 μg/mL of AIEE LP(DCDCS) into each sample and measured the PL spectra invisible region (for DCDCS emission) and near 1000 nm (for QC emission). The emission spectrum of DCDCS was clearly red-shifted and enhanced by about a factor of 5 upon mixing with the Tb^{3+} doped NPs, which indicates the formation of DCDCSs aggregates on the surface of the NPs. With the sensitization, we observed remarkably enhanced absorption in the ultraviolet region and PL at 980 nm for all of the Tb^{3+}-doped NPs (Figures A.3.3b). Plotting the integrated near IR (NIR) emission peak area of each sample(with and without DCDCS), demonstrated the extraordinary enhancement achieved with AIEE sensitization. For the 12%Tb^{3+} doped NPs, we observed a 2260-fold enhancement of emission intensity. For possible further optimization, we coated $NaYF_4$ shells of different thicknesses onto $NaYF_4$:50%Yb^{3+},12% Tb^{3+} cores and measured their emission with and without DCDCS. The PL intensity of pristine nanoparticles increased with increasing shell thickness. However, this trend was reversed upon adding DCDCS, illustrating the strong (r^6) distance dependence of FRET. From the relationship between the shell thickness and the FRET-induced QC emission intensity, we estimated the FRET radius between the DCDCS aggregate and $NaYF_4$:50% Yb^{3+}, 12% Tb^{3+} NPs as 2.56 nm. Because the QC emission intensity depends on the doping concentration of Tb^{3+} (Figure A.3.3c) and the inert shell thickness, we can rule out another possible energy transferring pathway in this system such as direct Dexter transfer from DCDCS to Yb^{3+}. The result of stronger emission without a shell suggests that the AIEE sensitizers improve the emission of the NPs through not only enhanced absorbance but also by passivation of trap sites on the NP surface, a function typically performed by an undoped shell. The contribution of passivation to enhanced emission was studied by exciting $NaYF_4$:50% Yb^{3+}, 12% Tb^{3+} NPs, with and without AIEE LP, at 920 nm, a wavelength that directly excites Yb^{3+} ions. These measurements showed a ~1.6-fold enhancement after coating the NPs with AIEE LP. Because the AIEE LP does not absorb at 920 nm (Figure A.3.1c), we attribute the 1.6-fold enhancement to passivation of the NP surface. Therefore, of the total 2260-fold enhancement, a change of around 1.6-fold originates from surface passivation, and the remaining 1410-fold enhancement is attributed to AIEE LP sensitization.

To further elucidate the mechanism of AIEE-dye-sensitized quantum cutting, we measured the emission intensity at 980nm of DCDCS-Tb^{3+}/Yb^{3+} NPs under 405 nm laser illumination as a function of the excitation power. When plotted on a log−log scale, the power dependence was fit well by a line with slope 0.69 (Figure A.3.3d), consistent with a QC process, for which typical values range from 0.5 to 1. Subsequently, we studied the QC emission intensity per nanoparticle as a function of the number of DCDCS molecules per NP. The PL intensity per NP was calculated by simply dividing the overall PL intensity by the number of nanoparticles.

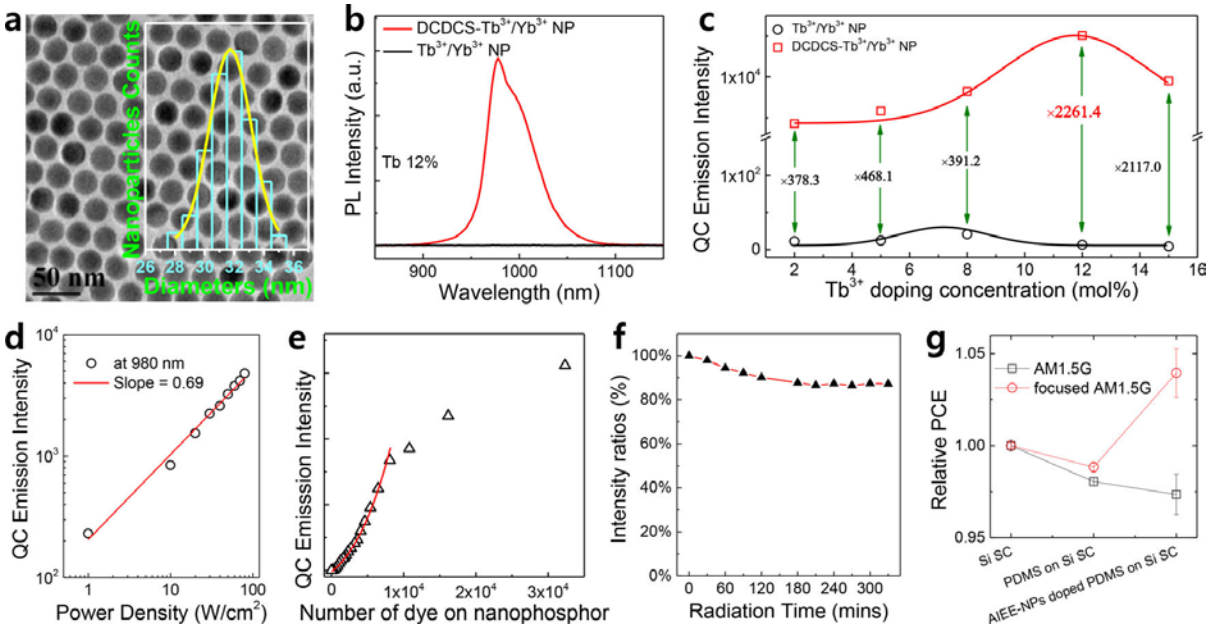

Figure A.3.3. AIEE-sensitized QC. (a) TEM and histogram of size distribution for YF_4:50%Yb^{3+},12%Tb^{3+} nanoparticles. (b) QC emission spectra of $NaYF_4$:50%Yb^{3+},12% Tb^{3+} nanoparticles with or without 100 μg/mL of DCDCS in $CHCl_3$/DMF (1:1) solution. (c) Integrated QC emission of $NaYF_4$:50%Yb^{3+}, x% Tb^{3+} (x = 2, 5, 8, 12, and 15) nanoparticles with or without 100 μg/mL of DCDCS in CHCl3/DMF (1:1) solution. (d) Excitation (405 nm) power dependence of QC emission at 980 nm for $NaYF_4$:50% Yb^{3+}, 12%Tb^{3+} nanoparticles with 100 μg/mL of DCDCS. (e) QC emission intensity as a function of the number of DCDCS molecules per $NaYF_4$:50% Yb^{3+}, 12% Tb^{3+} nanoparticle. For all of the QC emission measurements, a 405 nm laser was used as the excitation source. (f) Photostability of AIEE-sensitized QC. The graph represents time-dependent QC emission intensity upon continuous illumination with a 405 nm laser (190 W/cm2) in CHCl3/DMF (1:1) solution. (g) Relative PCE of bare and PDMS (with or without DCDCS-NPs)-covered Si SC under focused (780 mW/cm^2) or unfocused (100 mW/cm^2) AM1.5G illumination.

As shown in Figure A.3.3e, single-nanoparticle QC emission intensity increases exponentially with increasing dye content, from 0 to around 8000 molecules per NP and then begins to saturate. This clearly differentiates AIEE sensitization from sensitization with conventional LPs, for which PL intensity per NP declines beyond some critical number of sensitizers per NP. For AIEE dye to NP ratios from 0 to around 8000, the surface of the nanocrystals may not be fully covered by AIEE dye. Thus, the exponential growth can be attributed to aggregation-induced PL enhancement as the dye coverage on the QCNPs increases. This nonlinear PL enhancement is consistent with the typical AIEE enhancement upon aggregation in a mixed-solvent system. Somewhere near an AIEE dye to NP ratio of 8000, the surface of QCNPs is fully covered by DCDCS, with each dye molecule occupying ~0.4 nm^2 on the NP surface. A rough calculation (semiempirical (PM3)) for aggregated adsorbed DCDCS yields footprints of 0.65, 0.16, and 1.05 nm^2 for lateral, vertical, and parallel adsorption, respectively. Thus, combined experimental and theoretical considerations suggest that DCDCS are mainly adsorbed on NPs laterally, anchored by the two carboxylic acid groups. The slightly smaller average area observed experimentally could be attributed to the dynamic interaction between

the dye and NP. The increase in FRET between AIEE dye and Tb^{3+}increases more slowly beyond the point where full coverage of laterally adsorbed dyes is reached.

The FRET process was characterized with DCDCS and the $NaYF_4$ NPs with or without the doping of 50% Yb^{3+}/12%Tb^{3+}. The fluorescence of DCDCS on Yb^{3+}/Tb^{3+}-doped NPs was weaker than that on undoped (blank) NP, demonstrating the energy transfer from DCDCS to $NaYF_4$:50% Yb^{3+}, 12%Tb^{3+} QCNPs. To estimate the energy-transfer efficiency, the lifetime variation was fitted, showing a reduction from 3.7 to 1.8 ns. We can estimate the energy transfer efficiency from ET = $1-\tau_{DA}/\tau D$ (τ_{DA} and τ_D are the effective lifetimes of DCDCS in the absence and the presence of Tb^{3+}/Yb^{3+} doping) to determine an energy-transfer efficiency of 51%. Based on the PLQY of DCDCS (47%),the FRET efficiency (51%), and theoretical efficiency of QC between Tb and Yb (188%), we could estimate the whole energy-conversion efficiency to be up to 45%. Notably, the AIEE-sensitized QC system showed good stability; the QC emission intensity decreased by only 14% upon continuous illumination with a 405 nm laser (power density of 190 W/cm^2) for 5.5 h (Figure A.3.3f). Furthermore, the emission intensity of DCDCS, upon continuous UV illumination (365 nm, 0.3mW/cm2) and heating at 100 °C, for more than 20 hours decreased by less than 20%. This stability is far superior to the well-known indocyanine green sensitization system and, hence, increases the potential for practical applications.

We next demonstrated that the high UV to 980 nm photonconversion efficiency by AIEE sensitized QC is sufficient to improve photovoltaic performance by converting underutilized UV and blue photons to near-infrared photons that are more efficiently used by a silicon solar cell (Si SC). A crystalline Si SC can convert 800–1000 nm light to electric current more efficiently than visible light; however, much of the energy in the solar spectrum is at shorter wavelengths that are less efficiently utilized. This mismatch is one key factor limiting the conversion efficiency of photovoltaic cells. For instance, the maximum possible conversion efficiency (Shockley–Queisser limit) of Si SC with a bandgap of 1.1 eV under AM1.5 illumination is approximately 31%. With AIEE-sensitized QC, one UV high energy photon can be converted into two NIR photons, which the Si SC utilizes more effectively, in principle allowing efficiencies that exceed the Shockley–Queisser limit. As a first test of this application, we prepared thick films (2 mm) of DCDCS-NP-doped polydimethylsiloxane (PDMS). The transmittance spectrum of the PDMS film with DCSCS-NPs showed 2% lower transmission of incident light than that of the pristine PDMS in the efficient photocurrent generating wavelength range (400−1100 nm) of the Si SC, which is attributable to the light scattering by the NPs. It clearly showed an absorption band below 400 nm due to DCDCS. We put the film on a commercial Si SC and measured photovoltaic performance. Under unfocused (1 sun) AM1.5G simulated solar illumination, we did not observe any improvement in efficiency. In this case, nondirectional scattering by the nanoparticles caused light loss. We overcame this problem by focusing light upon the center of the device. Notably, with the focused AM1.5G illumination, the device with a DCDCS-NP doped PDMS film exhibited enhanced power-conversion efficiency (PCE) with a maximum of 8% relative increase and an average of 4% relative increase (Figures A.3.3g) of the original PCE, while pristine PDMS reduced the performance of the Si SC. We further measured the photostability of DCDCS-NPs again under

continuous illumination with focused AM1.5G for 6 h and observed less than 10% attenuation of QC emission over this time. This demonstrates the potential to achieve PCE improvement through spectral matching by AIEE-sensitized QC.

A.4. Subcellular optogenetic neuro-modulation with upconverted near-Infrared light

Optogenetic techniques have been developed to control the activities and functions of neurons and to probe the interconnection of neurons activities. When neural cells are excited by a specific wavelength of light, ion channels that are expressed with microbial opsins after viral transduction or transgenesis can activate or silence neuronal activity. However, a lot of common opsins are limited as their photoactivation requires visible light or ultraviolet light, which poorly penetrates through biological tissues due to high absorption and scattering by biomolecules.

Here, we report a new type of core/shell UCNPs, which upconvert the incident NIR light into blue emissions with exceptional efficiency. The $NaYbF_4$ core absorbs NIR light and the excitation energy migrates in the Yb^{3+} sublattice to reach the lanthanide emitters, ions of Tm^{3+}, producing selective blue UCPL. An epitaxial shell layer of $NaYF_4$ was deposited onto the core to passivate lattice defects on the surface and to spatially isolate the core nanoparticle from quenching centers in the surrounding medium. The UCPL output of the hexagonal core/shell ($NaYbF_4$:Tm)/$NaYF_4$ UCNPs presented here is exceptionally high, about 6× higher than the typically established hexagonal core/shell ($NaYF_4$:30%Yb/0.5%Tm)/ $NaYF_4$ UCNPs. Next, we demonstrated the breakthrough potential of novel UCNPs in optogenetics. We treated live cells expressing ChR2 with UCNPs conjugated with targeting ligand, folic acid (FA). After FA-conjugated UCNPs were internalized to produce upconversion, cells were irradiated with NIR light at 980 nm. We show that the upcoverted blue light activates opsins, allowing for controlling ion channel activity (Figure A.4.1). Whereas, in previous studies, optogenetic control over the membrane potential was mediated by upconversion material present in the substrate of cultured cells, our study demonstrated that optogenetic control could be mediated by UCNPs specifically targeted to cells. Moreover, owing to their exceptional upconversion efficiency and cell targeting ability, UCNPs are shown to provide for localized activation of ChR2 with a high subcellular precision. While the direct photoactivation with 476 nm light activates a large pool of opsins in the cellular membranes, as illustrated by bursts of Ca^{2+} in the entire cellular volume, the upconverted light activates predominantly those opsins, which are localized closely to intracellular UCNPs. Moreover, the scale of activation is proportional to the amount of UCNPs taken up by cells. In perspective, the reported here nanophotonics approach can advance subcellular optogenetics, which is a rapidly emerging discipline focused on control of cellular functions, as well as provide unprecedented opportunities for noninvasive control over neuronal circuitry in central neural system of live animals.

The UCNPs produce several UCPL bands, which could be used for selective photoactivation as well as for bioimaging applications. The emission of UCNPs is determined by the selected type of lanthanide dopants or their combinations. In UCNPs, typically, the doped Yb^{3+} ions (sensitizers) absorb infrared radiation and nonradiatively transfer excitation to

the doped activators X^{3+} (X = Er, Ho, Tm) to produce visible and ultraviolet upconversion luminescence (UCL). The $NaYbF_4$:Tm^{3+} 0.5% is selected as the core nanocrystals, not only because the energy transfer efficiency between the sensitizer Yb^{3+} ion and the emitter Tm^{3+} ion is demonstrated to be the highest, but also since the $NaYbF_4$ matrix can provide the most abundant Yb^{3+} ion concentration for strongest NIR excitation light harvesting at ~980 nm, which can then transfer to Tm^{3+} ion to produce blue UC PL. The epitaxial β-phase (hexagonal phase) ($NaYbF_4$:Tm^{3+} 0.5%)@$NaYF_4$ core/shell UCNPs were synthesized as described in the; the shell of $NaYF_4$ was selected due to its low lattice mismatch to the $NaYbF_4$ matrix. As shown in the transmission electron microscopic (TEM) images, the resulting UCNPs were uniform, of regular spherical shape, and ~50 nm in the diameter (Figure A.4.2a). Within each UCNP, a ~30 nm electron dense core coated with a ~10 nm light shell can be clearly resolved, demonstrating the formation of a core/shell nanostructure. We attribute this contrast to a large difference in the atomic number between the Yb^{3+} at the core (in the $NaYbF_4$ host lattice) and the Y^{3+} at the shell (in the $NaYF_4$ host lattice), resulting in different electron scattering cross-section.

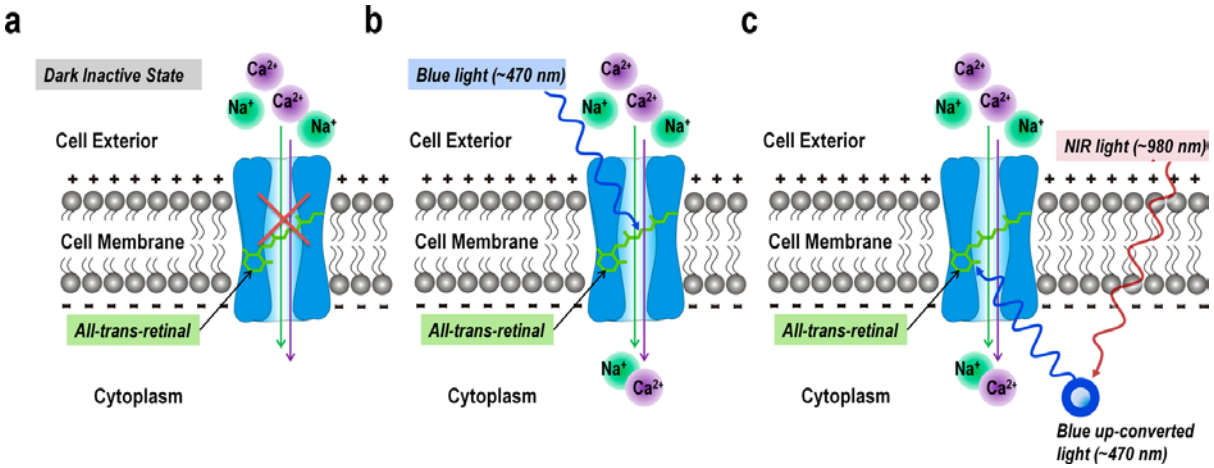

Figure A.4.1. Schematic representation of the optogenetic activation of neuronal signaling, wherein ion channel protein ChR2 is inserted into cellular membrane. ChR2 opens for intracellular influx of Ca^{2+} and Na^{+} upon activation with blue light (~470 nm), which results in membrane depolarization and neuronal signal firing. (a) ChR2 channel is inactive at dark. (b) Activation of ChR2 channel for Ca^{2+} and Na^{+} import by blue light irradiation. (c) Photon nanotransformers, internalized into the cell, upconvert incident NIR light (980 nm) into blue light at ~470 nm for activation of the ChR2 channel.

The crystallographic phase has a strong impact on the efficiency of UCPL. A lower crystal phase can favor higher UCPL efficiency, as a low symmetry crystal filed can relax more dipole forbidden nature of 4f−4f transitions. Indeed, it has been shown that $NaYF_4$:Yb^{3+}/Er^{3+} microsized particles of hexagonal phase are about ~10× more efficient than its cubic form particles. Though the hexagonal phase $NaYF_4$ nanoparticles have been prepared using various chemistry, it is nontrivial to prepare uniform Tm^{3+}-doped hexagonal $NaYbF_4$ nanoparticles due to its distinct growth dynamics from the hexagonal $NaYF_4$ nanoparticles. To achieve this, we used a two-step thermolysis protocol adapted from a recent work. The first step is to prepare cubic phase irregular $NaYbF_4$nanoparticles, which are then converted into uniform hexagonal phase nanoparticles using the Ostwald-ripening confined process in the second step. A third seed-mediated epitaxial growth enables the preparation of the shell layer with the hexagonal

phase.

Next, the optical properties of the obtained UCNPs were studied. The UC PL spectra of the resulting $NaYbF_4$:Tm^{3+}0.5% core, and core/shell ($NaYbF_4$:Tm^{3+} 0.5%)@$NaYF_4$aredisplayed in Figure A.4.2b, along with referenced canonical($NaYF_4$:Yb^{3+}30%/Tm^{3+} 0.5%)/$NaYF_4$particles, which up to date have been considered to be the most efficient UCNPs, with an upconversion quantum yield of ~3.5%.These nanoparticles were dispersed in hexane under identical concentrations for the comparison. The UC PL peaks at 358,450, 470, 650, and 801 nm correspond to transitions between$^1I_6 \rightarrow {}^3F_4$, $^1D_2 \rightarrow {}^3F_4$, $^1G_4 \rightarrow {}^3H_6$, $^1G_4 \rightarrow {}^3F_4$, and $^3H_4 \rightarrow {}^3H_6$of Tm^{3+} ions, respectively. As could be expected from the chemical formulation, the upconversion spectra of both types of UCNPs contained same peaks corresponding to the Tm^{3+}transitions. At the same time the upconversion efficiency of synthesized in our study UCNPs was significantly higher. We also documented a~6−8× higher levels of 450/470 nm UCPL in comparison with the canonical "gold standard" ($NaYF_4$:Yb^{3+}30%/Tm^{3+}0.5 %)/$NaYF_4$ particles (Figure A.4.2b). We conclude that the high upconversion efficiency of the characterized here UCNPs arises from a combined effect of highly efficient energy transfers from the sensitizer Yb^{3+} (enhanced by Yb^{3+}-induced to the activator Tm^{3+}, as well as an efficient suppression of surface-related quenching mechanisms. To confirm the later effect, the PL decay at 801 nm was measured for both samples shown in Figure A.4.2b.

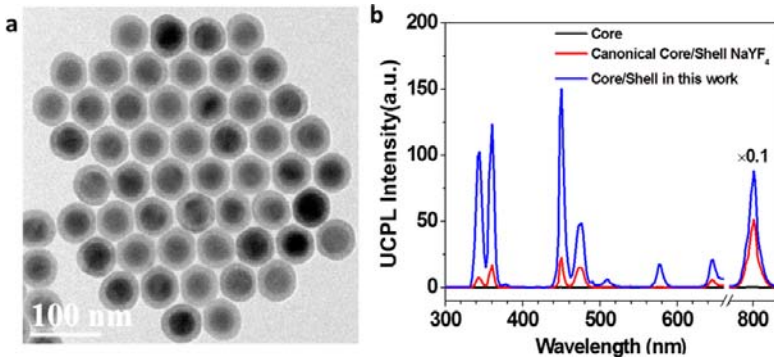

Figure A.4.2. (a) Transmission electron microscopy image of the synthesized ($NaYbF_4$:Tm^{3+} 0.5%)@$NaYF_4$ core/shell UCNPs. (b)UCPL of the core $NaYbF_4$:Tm^{3+}nanoparticles (black line), the designed in this study ($NaYbF_4$:Tm^{3+} 0.5%)@$NaYF_4$core/shell UCNPs (blue line), as well as the referenced canonical hexagonal phase ($NaYF_4$:Yb^{3+}30%/Tm^{3+} 0.5%)/$NaYF_4$ UCNPs (~30−40 nm).

Next, we explored the utility of the developed UCNPs for optogenetic applications, wherein a control over cellular signaling is executed via NIR-to-blue upconversion light from the UCNPs that were internalized into live cells (Figure A.4.1c). In these experiments, cells were transfected with a genetic construct coding for fusion of ChR2 and Enhanced Yellow Fluorescent Protein (EYFP). Upon synthesis and maturation, this EYFP tethered opsin relocates to the cell membranes, hence, the successfully transfected cells could be identified by the fluorescence signal from EYFP. At the beginning, the functionality of ChR2 was validated under direct activation with blue light, using 476 nm laser source. To detect opening of ChR2 ion channels, cells were loaded with Asante Calcium Red AM (ACR), a cell permeable fluorescence indicator of Ca^{2+}.ACR can be excited at ~540 nm and generate, in the presence of Ca^{2+}, a fluorescence emission peak at 650 nm, where no measurable interference from cellular

autofluorescence is present.

In our experiments, cells were simultaneously scanned with two laser beams, one at 476 nm to activate ChR2 channel, and the other at 543 nm to excite ACR. In this experimental design, the 476 nm laser line was periodically switched on/off (FigureA.4.3). The excitation pulses were spaced apart with lags of several seconds, for deactivation of ChR2 and recovery of the membrane potential. At the same time, cells were scanned continuously with the 543 nm laser line, to excite ACR for monitoring changes in the intracellular Ca^{2+} signal in response to the opening and closing of opsin channels. We observed that cells responded to irradiation in a timely manner with 476 nm light, demonstrating a corresponding increase of the Ca^{2+} signal within several tens of milliseconds (Figure A.4.3), which isconsistent with reported data.

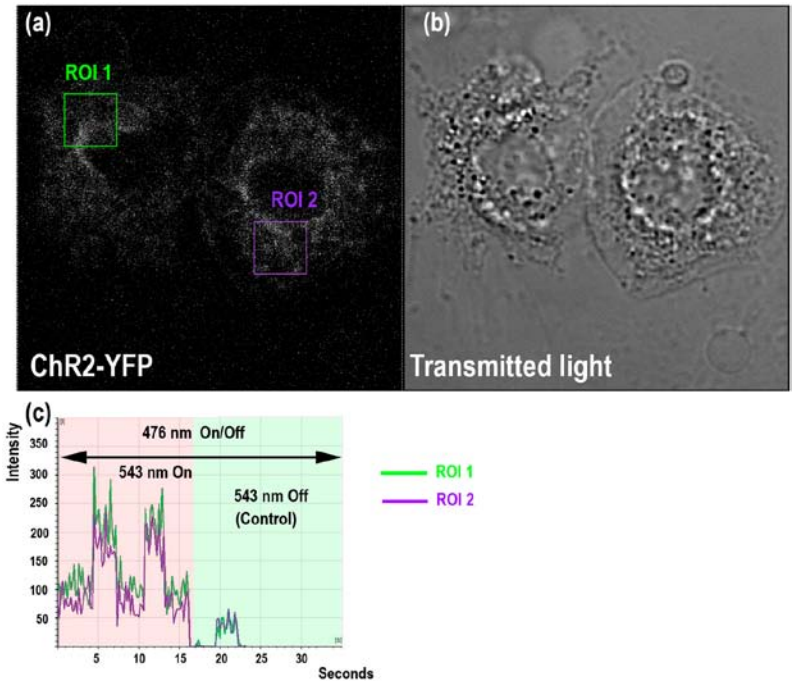

Figure A.4.3. Direct activation of ChR2 protein in cellular membranes with 476 nm light. (a) Cells expressing ChR2 in cellular membranes visualized by YFP tag. (b) Transmitted light images of the same cells. Influx of Ca 2+ in response of ChR2 activation with 476 nm light was measured in two rectangular Region of Interests, ROI 1 and ROI 2, as indicated. (c) Comparative measurement of fluorescence intensity in the ACR spectral region with 476 and 543 nm light on and off.

Furthermore, we addressed a common methodological problem of overlapping signals between most Ca^{2+} reporters and a broad spectrum from the YFP tag of ChR-2. Because of this overlap, the YFP signal typically contributes to the fluorescence obtained from Ca^{2+}dyes, which requires carrying stringent control experiments to verify that the measured changes in the fluorescence intensity exceed contribution from YFP. In our study, we performed control experiments by turning off 543 nm laser. Under these experimental conditions, the contribution of YFP signal to the spectral range (600−640nm) of ACR emission was identified.

The efficiency of light-induced activation varied from cell-to cell. Typically, the elevation of ACR signal correlates with the abundance of ChR2-YFP in the cellular membranes. At the same time, we found that changes in the intensity of ACR signal were significantly more pronounced for cells growing in the NMDG containing buffer. On the average, the changes in fluorescence signal from ACR were three to four fold higher than those from YFP, which confirmed the light-gated control of the ChR2 ion channel using 476 nm source (Figure A.4.3).

At the following stage of our study, HeLa cells were targeted with phospholipid-coated UCNPs. To ensure an efficient uptake of UCNPs by the cells, folic acid (FA) was used as a

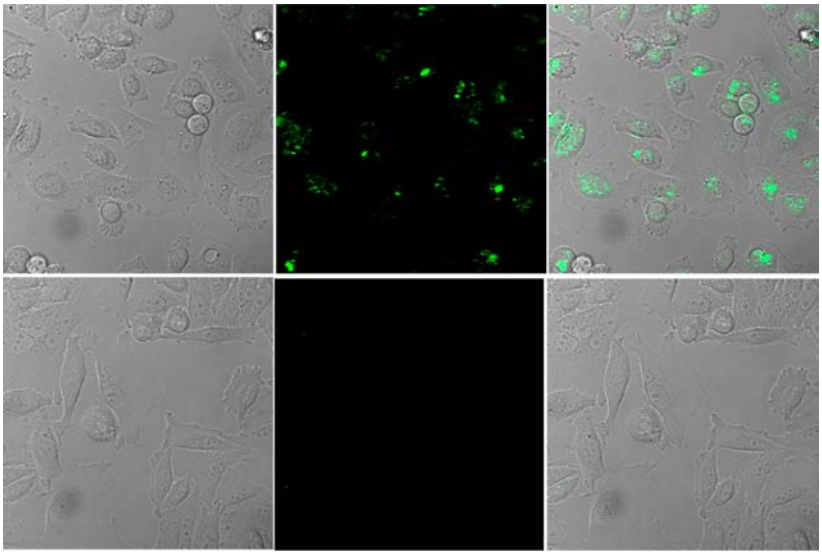

Figure A.4.4. Targeting UCNPs to cultured cells: FA-conjugated UCNPs (upper row) and nonconjugated UCNPs (bottom row). A striking difference between cellular uptake for the FA-conjugated and nonconjugated UCNPs is apparent.

ligand for specific targeting of cancer cells with enhanced expression of FA receptors. We found that FA-mediated targeting was highly effective, resulting into significant intracellular uptake of UCNPs, while almost no intracellular signal was found for nontargeted particles (Figure A.4.4). These data indicate that functionalization of UCNPs for recognition of various cellular receptors may enable incorporation of nanoformulations into specific cellular types, such as various types of neurons. Using confocal laser scanning microscopy, we could resolve UCNPs inside the treated cells, at the same time cellular morphology was not noticeably affected (Figure A.4.4). Consistently, we did not detect any significant impact of UCNPs on the cellular viability (data not shown) using standard MTS assay as described elsewhere.

To activate ChR2 through upconversion of NIR light, cells were irradiated by a 980 nm CW laser source. As could be seen in Figure A.4.2b, the emission of UCNPs peaked at 450/470 nm, falls within the maximum absorption of ChR2. Hence, we utilized these upconversion bands to activate ChR2 protein in membranes of live cells. Simultaneously, these cells were irradiated at 543 nm to monitor the changes in intensity of ACR signal in response activation/deactivation of ChR2.

We found that the NIR excitation at 980 nm (gated by mechanical shutter), upconverted on UCNPs to blue light, timely coincided with the significant increases of ACR fluorescence. The highest fluorescence response was observed in the cells incubated in the NMDG buffer (Figure A.4.5).

Cells with the highest number of internalized UCNPs demonstrated nearly as high increase in ACR fluorescence as in the experiments with direct activation of ChR2 at 476 nm (Figure A.4.3), which points toward high efficiency of UCNPs for activation of opsins. Meanwhile, cells with a lower number of targeted UCNPs demonstrated a correspondingly lower influx of Ca^{2+} upon excitation with NIR light (Figure A.4.5d,e).This finding suggests that optogenetic activation can be limited to populations of neurons by targeting UCNPs to specific cellular types, whereas any significant stimulation of the nontargeted cells is not expected. Furthermore, the specific targeting along with the excitation of lower power density may allow for use of UCNPs in unsaturated regime. As a result, multiphoton dependence on the excitation power can be exploited for UCPL, allowing to stimulate the selected cell populations in depth, similar

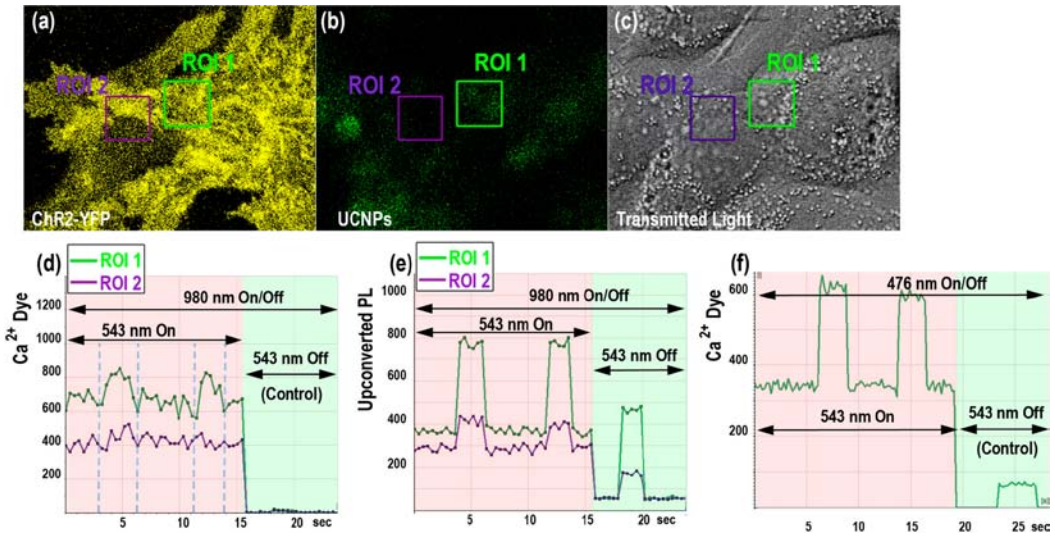

Figure A.4.5. (a) Activation of ChR2 in HeLa cells maintained in NMDG buffer by upconverted NIR light or by 476 nm excitation. (a–c) Microscopic images of HeLa cells expressing ChR2-YFP and loaded with UCNPs. Panels correspond to (a) ChR2-YFP, (b) UCNPs, and (c) transmitted light images, as indicated. Two regions of interest (ROI), with different amounts of UCNPs are marked as green and purple squares. The accumulation of UCNPs is seen to be much higher in ROI 1 than in ROI 2. (d, e) Activation of ChR2 by 980 nm light. (d) Changes in Ca^{2+} signal intensity in response to exposures to 980 nm light for two ROIs. (e) Upconversion photoluminescence measured in ROI 1 and ROI 2 simultaneously with (d). The upconverted PL peaks in (e) coincide with the peaks of Ca^{2+} signal, marked by dashed lines in (d). (f) Activation of ChR2 by 476 nm light. Changes in the ACR intensity in the same cell, in response to 476 nm impulses.

to the two-photon induced optogenetics.

Moreover, we found that the influx of Ca^{2+} ions in different parts of the cell correlated with the subcellular concentration of UCNPs (Figures A.4.5). Changes in Ca^{2+} signal intensity were recorded only in proximity of UCNPs, while no activation of ChR2 was detected in the regions of the same cell, which did not contain a significant number of these nanoparticles (Figure A.4.5d,e).

In comparison with direct activation of ChR2 by blue light, which induces very significant changes in the ACR signal in entire cellular volume (Figure A.4.5e), activation by upconverted PL was found to not as significant and limited to the cellular domains with UCNPs. It is worth noting, that during the activation of ChR2 in the cell, using laser scanning microscope, the laser excitation beam stays in every pixel for few microseconds. Therefore, in the laser scanning experiment, the efficiency of UCNPs-mediated activation is inherently limited.

We believe that high localization of UCNP-mediated photoactivation represents great potential for subcellular optogenetics, which is an emerging direction in studies of cellular signaling activities. Since NIR light is not significantly absorbed by cellular biomolecules, the incident irradiation in the absence of UCNPs is not likely to trigger any cellular response. Meanwhile, it is feasible to target UCNPs to specific cellular compartments, by functionalization with various ligands,which would enable for spatially precise activation of photoprocesses in the sites of their subcellular localization. Potential applications may include regulation of intracellular Ca^{2+} release from the endoplasmic reticulum, regulation oforganelle-bound enzymes and

control of gene activities. Furthermore, the versatility of UCNPs can also be leveraged in the creation of a multifunctional reagent that will deliver genetic material coding for optogenetic proteins to a target cell and then subsequently act to upconvert light to the appropriate opsin-activating wavelength.

A.5. Tunable Narrow Band Emissions from Dye-Sensitized Core/Shell/Shell Nanocrystals in the Second Near-Infrared Biological Window

We developed a hybrid organic–inorganic system consisting of an epitaxial $NaYF_4:Yb^{3+}/X^{3+}@NaYbF4@NaYF_4:Nd^{3+}$ (X =null, Er, Ho, Tm, or Pr) core/shell/shell (CSS) nanocrystal with organic NIR dyes (indocyanine green, ICG) attached to the CSS nanocrystal surface. This hybrid system is able to produce efficient multicolor narrow-band NIR-II emissions with excitation across a broad spectral range (Figure A.5.1b), allowing imaging through thick biological tissues. The structure of ICG-sensitized CSS nanocrystal is depicted in Figure A.5.1a, whereby ICG (absorption cross section of 10^{6} cm $^{-2}$) can harvest NIR light in a broad range, entailing a wide excitation spectral range (700–860 nm). The harvested energy is then nonradiatively transferred to the Nd^{3+} ions in the outer shell layer, then to the Yb^{3+} ions in the inner shell layer, and finally to the Yb^{3+}/X^{3+} ion pair (X = null, Er, Ho, Tm, or Pr) in the inorganic core to entail a plethora of emitter-defined narrow emissions in the NIR-II range (Figure A.5.1a). The CSS structure employed here not only suppresses surface-related quenching of the core nanocrystal by spatial isolation from the environment but also elicits directional energy flow all the way to the core nanocrystal to emit large Stoke-shifted NIR-II emission.

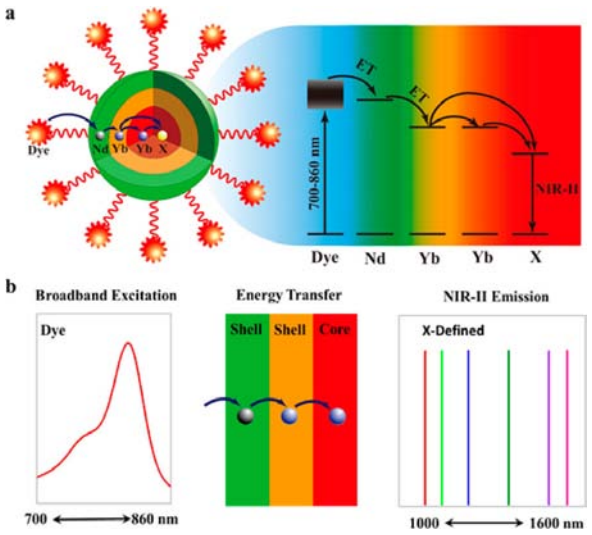

Figure A.5.1. Schematic illustrations of (a) energy transfer pathway from ICG on the surface of $NaYF4:Yb^{3+}/X^{3+}@NaYbF_4@NaYF_4:Nd^{3+}$ nanocrystal, to the Nd^{3+} ions in the outer shell, then to the Yb^{3+} in the inner shell, and finally to the Yb^{3+}/X^{3+} (X = null, Er, Ho, Tm, or Pr) in the core, producing large Stokes-shifted NIR-II emissions. (b) the functional roles of ICG (providing excitation between 700 and 860 nm, absorption spectrum for 40 μg/mL in DMF), the core/shell/shell structure (spatial isolation of the core from surrounding quenching center, and directing energy transfer to the core), and the activator of varying type (entailing defined

Hexagonal $NaYF_4$ with low phonon energy is chosen as the inorganic host material to build the CSS structure because it is known to be one of the most efficient materials for lanthanide emission. CSS nanocrystals of $NaYF_4$:30%Yb^{3+}/2%X^{3+}@$NaYbF_4$@$NaYF_4$:30%Nd^{3+} (X = null, Er, Ho, Tm, or Pr) were synthesized following an adapted procedure from theliterature.28 Transmission electron microscopy (TEM) results(Figure A.5.2a) show that the

NaYF4:Yb^{3+}/X^{3+} core, the$NaYF_4:Yb^{3+}/X^{3+}$@$NaYbF_4$ core/shell, and the $NaYF_4:Yb^{3+}/X^{3+}$@NaYbF4@$NaYF_4:Nd^{3+}$ CSS nanocrystals are spherical and uniform, with a mean size of 32, 43, and 52 nm, respectively. This suggests that each shell layer has a thickness of ~ 5 nm for the CSS nanocrystals. X-ray diffraction (XRD) results indicate that the core, the core/shell, and the CSS nanocrystals are of hexagonal crystallographic phase with good crystallinity. When excited at ~ 800 nm, the CSS nanocrystals of$NaYF_4$:30%Yb^{3+},2%X^{3+}@$NaYbF_4$@$NaYF_4$:30%Nd^{3+} (X = null, Er, Ho, Tm, or Pr) are able to emit multiple narrow band emissions with a large Stokes shift (>200 nm) at 1000 nm forYb^{3+} (X = null), 1165 nm (X = Ho), 1310 nm (X = Pr), 1460 nm(X = Tm), and 1530 nm (X = Er) (Figure A.5.2b),respectively. The emission at 1060 nm of Nd^{3+} from $NaYF_4:Nd^{3+}$ nanocrystals is included in Figure 2b as a reference. These narrow emission peaks cover the whole spectral range between 1000 and 1600 nm, implying their suitability for multiplexed bioimaging in the NIR-II region. Note that the existence of the $NaYbF_4$ layer in the CSS structure is important to maximize emission from the emitter X, as this layer can suppress detrimental cross-relaxation processes between X and Nd^{3+} by spatial isolation, and enhance energy transfer from the outer shell to the core by introducing Yb-mediated energy migration.

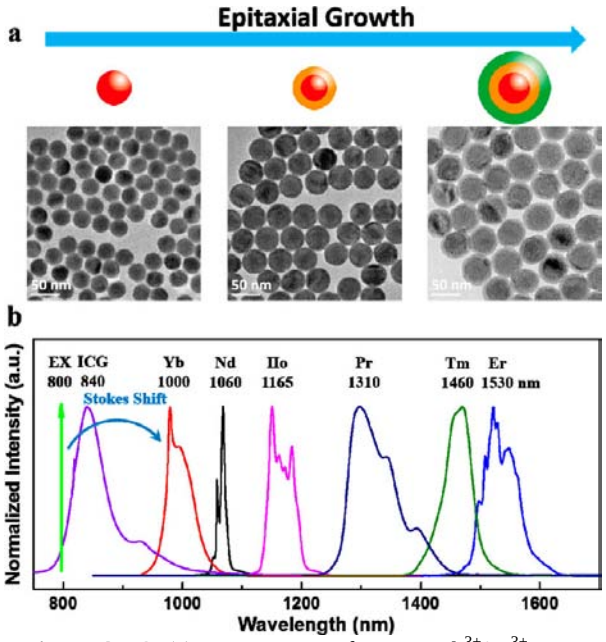

Figure A.5.2. (a) TEM images of $NaYF_4:Yb^{3+}/Er^{3+}$ core, $NaYF_4$:Yb,Er@NaYbF4 core/shell, $NaYF_4:Yb^{3+}/Er^{3+}$@NaYbF4@NaYF4:Nd^{3+} core/shell/shell nanocrystals (from left to right). (b) Normalized multiband NIR-II emission peaks from nanocrystals of $NaYF_4:Yb^{3+}/X^{3+}$@$NaYbF_4$@$NaYF_4:Nd^{3+}$ (X = null, Er, Ho, Tm, or Pr) dispersed in hexane (1 wt %). The emission peak at 1060 nm from hexane-dispersed $NaYF_4:Nd^{3+}$ nanocrystals is added as a separate NIR-II emission band. Excitation at 800 nm with a power density of 4 W/cm^2.

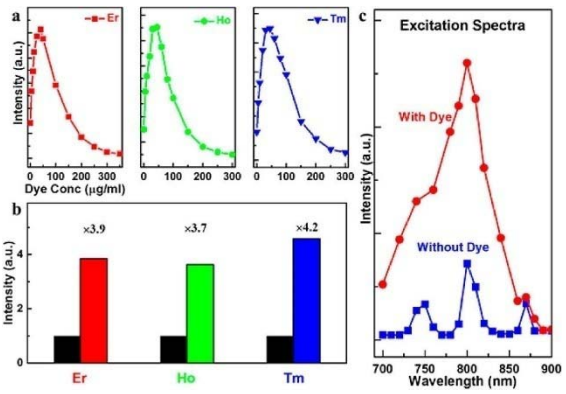

Figure A.5.3. (a) Dependence of the integrated emission intensities from the $^4I_{13/2}$ level of Er^{3+} (1530 nm), from the $^5I_6$ level of Ho^{3+} (1165 nm), and from the $^4H_4$ level of Tm^{3+} (1460 nm) of ICG-sensitized CSS nanocrystals versus the ICG concentration. (b) Histogram shows the comparison of integrated emission intensities from Er^{3+}-, Ho^{3+}-, or Tm^{3+}-doped CSS nanoparticles with and without (NOBF4-capped) ICG sensitization (the intensities without dye sensitization were normalized for clarification). (c) Photoluminescent excitation spectra (for the integrated emission intensity from the $^4I_{13/2}$ state of Er^{3+}) for Er^{3+}-doped CSS nanocrystals with and without ($NOBF_4$-capped) ICG sensitization.

We then investigated the sensitization effect of ICG on the CSS nanocrystal to impart a broad excitation spectral range and enhance the brightness, aiming to facilitate the use of these nanoparticles in optical imaging. We selected ICG because of its high NIR luminescence efficiency and the strong overlapping of its emission spectrum with the absorption spectrum of Nd ions. The long-chain ligand of oleic acid (OA) used during synthesis of CSS nanocrystals was first replaced by a short ionic ligand of nitrosonium tetrafluoroborate ($NOBF_4$) (no luminescence quenching was observed), followed by mixing with ICG to enable attachment to the nanocrystal surface through the tetrafluoroborate group. The introduction of ICG into the CSS nanocrystal dispersion is able to enhance the emission intensities of CSS nanocrystals, independent of the doped emitter (X) type. The dependency of the integrated emission intensity from CSS nanocrystals doped with emitter of Er^{3+} (1530 nm), Ho^{3+} (1165 nm), and Tm^{3+} (1460 nm) on ICG concentration are shown in Figure A.5.3a. The optimized ICG concentration was revealed to be ~40−45 μg/mL, which resulted in 3.9-, 3.7-, and 4.2-fold enhancement for the$NaYF_4$:30%Yb^{3+}/2%X^{3+}@NaYbF4@$NaYF_4$:30%Nd^{3+} CSS nanocrystals doped with X = Er^{3+}, Ho^{3+}, and Tm^{3+}, respectively (Figures A.5.3b). The efficiency of energy transfer from ICG to the nanoparticle was determined to be ~75%; while the luminescence quantum yield of ICG sensitized Er^{3+}-doped CSS nanoparticles was measured to be ~13%. The dependence of emission intensity on ICG concentration is possibly a result of the competition between the ICG dye antenna effect (enhancing light harvesting) and the dye-dye quenching interaction (deactivation of harvested energy) on the surface of the CSS nanocrystals. The 4-fold excitation intensity difference at 800 nm (Figure A.5.3c) is in good agreement with 4-fold emission enhancement induced by ICG sensitization in Figure 3b. Moreover, the broad-band excitation peak from ICG-attached CSS nanocrystals is in marked contrast to the sharp and narrow band peak from pure CSS nanocrystal, providing a direct evidence of ICG sensitization.

The significantly widened excitation spectrum permits these ICG-sensitized CSS to be excited within a broad spectral range from 700 to 870 nm, facilitating their applications with multiple different light sources.

The enhancement of emission intensity caused by the ICG sensitization effect can also be clearly seen by comparing the NIR-II photoluminescent image of ICG-sensitized CSS nanocrystals vs pure CSS nanocrystals (dispersed in DMF) using a NIR-sensitive InGaAs camera (New Imaging Technologies) (Figure A.5.4a). To test whether ICG-sensitized CSS nanocrystals are suitable for deep tissue optical bioimaging, we imaged the NIR-II luminescence of polymer pattern (the letter "A", 3 × 3cm) incorporating ICG-sensitized $NaYF_4$:30%Yb^{3+}/2%Er^{3+}@$NaYbF_4$ @$NaYF_4$:30% Nd^{3+} nanocrystals through tissue (chicken breast) of known thickness. The polymer pattern was made by mixing the ICG-sensitized CSS nanocrystals with polystyrene beads in chloroform to yield a transparent and uniform gel, followed by casting through a homemade mold with natural evaporation of the solvent. The green upconversion emission of Er^{3+} (~540 nm) from the same pattern was utilized as a control study (taken by a visible-sensitive camera), which previously was employed for upconversion bioimaging (FigureA.5.4b). The sharp image of the polymer pattern can be visualized by NIR-II emission with a tissue depth of up to 9 mm, and the emission signal can be detected even with a depth of up to 23 mm. However, both the letter image and the emission signal are hard to be detected when using green upconversion through tissue thickness of merely 3 mm under the same excitation at 800 nm (Figure 4b,d). This result clearly implies the appropriateness of NIR-II emission from ICG-sensitized CSS nanocrystals

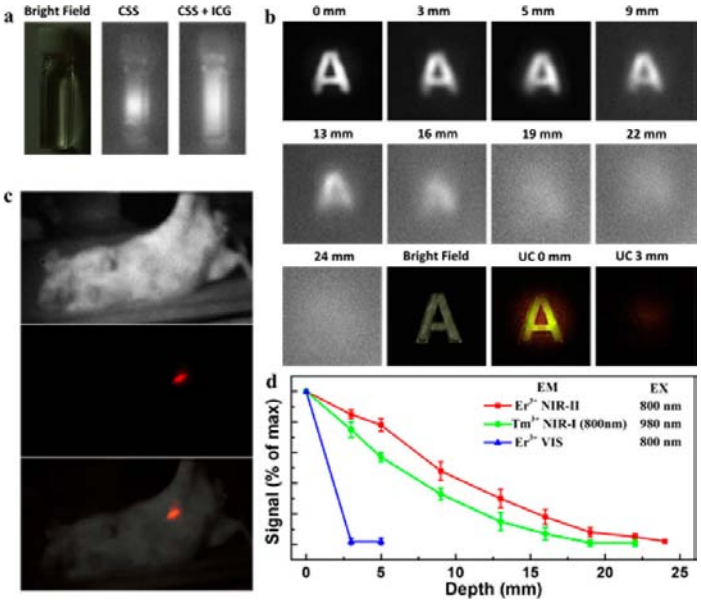

Figure A.5.4. (a) NIR-II photoluminescent imaging of Er^{3+}-doped CSS($NaYF_4$:30%Yb^{3+},2%Er@$NaYbF_4$@$NaYF_4$:30%Nd) nanocrystals with and without ICG sensitization (excited at 800 nm). (b) NIR-II photoluminescent image of the polymer pattern containing ICGsensitizedEr^{3+}-doped CSS nanocrystals through chicken breast tissue ofvaried thickness (excited at 800 nm). (c) NIR-II photoluminescentbioimaging of a mouse with subcutaneous injection (excited at 800 nm).(d) Detected intensity of NIR-II emission from ICG-sensitized Er^{3+}-doped CSS nanocrystals (excited at 800 nm), green upconversion emission (at ~540 nm) from the same nanocrystal (excited at 800 nm),as well as NIR-I upconversion emission (800 nm) from $NaYF_4$:30%Yb^{3+}/0.5%Tm^{3+}@$NaYF_4$ core/shell nanocrystals (excited at 980 nm),versus the imaging depth. The excitation density at both 800 and 980 nmis ~0.2 W/cm^2.

for deep tissue optical imaging. Moreover, it has been established that Yb^{3+}/Tm^{3+}-codoped upconversion nanocrystals are good for deep optical bioimaging, as both the excitation of ~ 980 nm and the upconverted emission at ~800 nm fall within the first biological window (NIR-I region). Next, we utilized the upconversion emission from typically used $NaYF_4$:30%Yb^{3+}/0.5%Tm^{3+}@$NaYF_4$ core/shell nanocrystals as a positive control to probe the deep tissue imaging ability of NIR-II emission from ICG-sensitized Er doped CSS nanocrystals (Figure A.5.4d). It was found that the NIR-II emission is better than upconverted emission at 800 nm for deep tissue optical imaging, by showing improved signal at all defined tissue depths, possibly owing to reduced photon scattering in the NIR-II window than in the NIR-I window. This conclusion was supported by the observation of a blurred upconversion image (NIR-I range) ofthe "A" pattern through a 5 mm thick tissue, compared to the sharp letter NIR-II NIR-II image through a 9 mm thick tissue (Figure A.5.4b). Moreover, the ability to resolve two NIR-II line images with a threshold distance of 3mmand two dot images with a distance of 4 mm through a 4 mm thick tissue suggests a lateral resolution ~3−4 mm at this imaging depth in biological tissues (organic phase particles were utilized). To demonstrate further the suitability of ICG-sensitized CSS nanocrystals for bioimaging, we employed an amphiphilic polymer DSPE-mPEG-2000 (1,2-distearoyl-*sn*-glycero-3-phosphoethanolamine-*N*-methoxy (polyethylene glycol)-2000) to encapsulate the ICG-sensitized Er doped CSS nanocrystals, thereby transferring them into the aqueous phase. Our hydrodynamic size measurement (over a period of 7 days), luminescence measurement (over 6 h), as well as HeLa cell viability test (dose of 0−1 mg/mL, 24 and 48 h) suggest that these aqueous forms are stable in vivo (but with a decreased luminescence intensity) and they exhibit negligible cytotoxicity. After subcutaneous injection of these aqueous suspended nanoparticles (0.2 mL of 2 mg/mL) into a mouse with a depth of ~3 mm, a clear NIR-II image of the injection point was obtained (Figure A.5.4c).

A.6. A core–multiple shell nanostructure enabling concurrent upconversion and quantum cutting for photon management

We developed a core–shell–shell–shell architecture of $NaYF_4$:10%Er^{3+}@$NaLuF_4$@$NaYF_4$:2%Tb^{3+},20%Yb^{3+}@$NaYF_4$nanoparticles for concurrent UC and QC implementation (Figure A.6.1b). We select the Yb/Tb pair to implement QC, as this ion couple is a classic model for the cooperative QC process. The resulting core–multishell nanoparticles were demonstrated to combine QC from UV (355 nm) and VIS (488 nm) to VIS and NIR, with UC from ~1.5 μm to VIS and NIR. The thickness of the $NaLuF_4$ layer was

varied in order to be employed as the "inert" layer for blocking the adverse cross-relaxation between the UC layer and the QC layer. First, we separately optimized doping concentrations of rare-earth ions that account for UC and QC processes in the $NaYF_4$host matrix which is considered to be one of the most efficient host materials, to obtain high efficiencies for both processes. The trivalent erbium ions (Er^{3+}) were selected as dopants for the UC process, while the trivalent ytterbium (Yb^{3+}) and terbium (Tb^{3+}) ions were selected as dopants for the QC process. Nanocrystals of $NaYF_4$ doped with Er^{3+} ions upconverting light at ~1.5 μm were well studied by us earlier; it has been determined that 10% of Er^{3+} is the optimized doping concentration to reach the highest UC efficiency in the $NaYF_4$ nanomatrix. To investigate the possibility for QC implementation within this nanomatrix, $NaYF_4$ nanoparticles co-doped with 2%Tb^{3+} and x%Yb^{3+} (x = 0, 20, 40, 60 and 80) were synthesized using a protocol adapted from our recent work. It is well known that the particle size (and the corresponding surface-to-volume ratio) determines the amount of surface related luminescence quenching, which impacts the UC and QC efficiencies tremendously. Varying the Yb^{3+} doping concentration can result in the formation of nanoparticles with distinct

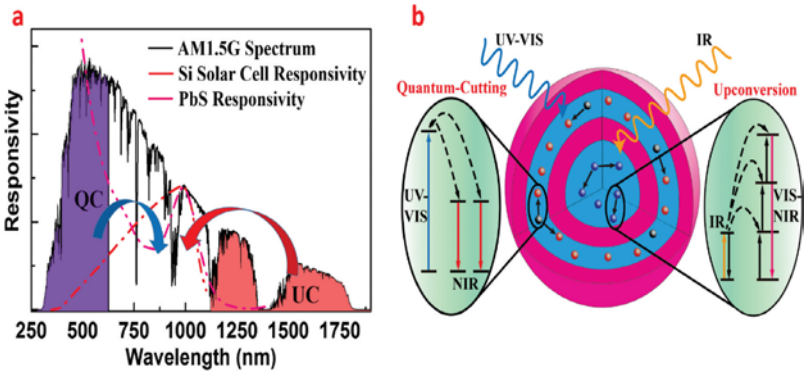

Figure A.6.1 (a) The AM1.5G solar spectrum versus the silicon photoresponsivity and the absorption of lead sulfide (PbS) quantum dots with excitation absorption peak at ~1000 nm, which are typically used for colloidal quantum dot solar cells and the inorganic–organic hybrid solar cells. A fraction of terrestrial sunlight unutilized or under-utilized for most solar cells has been highlighted and can be converted [through a quantum cutting (QC)process or an upconverison (UC) process] into the range where silicon or PbS quantum dots have a high sensitivity. (b) A proposed core/multishell nanostructure to realize both QC and UC processes in spatially confined regions for concurrent spectral conversion. UC occurs in the active core region (blue), while QC occurs in the second active shell layer (blue). The first inert layer (magenta) is utilized to inhibit the interference between the active domains, while the outmost inert third shell layer (magenta) is used to suppress surface-related quenching mechanisms by spatial isolation of the active domains from the environment.

sizes, due to the dopant-induced transient polarization effect during the particle growth process. To prepare nanoparticles doped with varied Yb^{3+} concentrations but of the same size, to exclude difference in the size-induced surface effects, we controlled the nanoparticle size by varying the amount of the coordinating ligand, oleic acid. The transmission electron microscopy (TEM) images of the synthesized nanoparticles are shown in Figure A.6.2a–e. The size of $NaYF_4$:2%Tb^{3+},x%Yb^{3+} (x = 0, 20, 40, 60 and 80) nanoparticles was found to be 42 ± 0.8, 43 ± 0.2, 42 ± 0.2, 43 ± 0.8, and 44 ± 2.2 nm, respectively, substantiating the uniform size of the synthesized nanoparticles. Note that the shape of these nanoparticles evolves from nanospheres to hexagons with the increase of Yb^{3+} ions. The X-ray diffraction (XRD) patterns in Figure A.6.2f confirm that the crystallographic structures of all nanoparticles are hexagonal. Under excitation at 355 nm, nanoparticles of $NaYF_4$:2%Tb^{3+},x%Yb^{3+} (x = 0, 20, 40, 60 and 80) manifest photoluminescence (PL) emission in visible and NIR ranges. Excitation at this wavelength populates the $^5D_3$ state of theTb^{3+} ions, followed by nonradiative relaxations of the Tb^{3+} ions to the $^5D_4$ state (see Figure A.6.6d). As shown in Figure A.6.3a, there are seven peaks in the range of 450–700 nm, which correspond to the $^5D_4 \rightarrow {}^7F_J$ (J = 6, 5, 4, 3, 2, 1 and 0) transition of the Tb^{3+}ions. The NIR PL band in the 900–1000 nm range can be ascribed to the $^2F_{5/2} \rightarrow {}^2F_{7/2}$ transition of the Yb^{3+} ions, since the nanoparticles without the Yb^{3+} ions ($NaYF_4$:2%Tb^{3+}) do not display NIR PL. The emission from the Tb^{3+} ions in the visible range becomes weaker with the increase in Yb^{3+}doping, suggesting more efficient excitation energy transfer(ET) from Tb^{3+} to Yb^{3+}. At the same time, the NIR PL intensity decreases with an increase in the concentration of Yb^{3+}, which implies a competition between the ET-induced enhancement and the Yb^{3+} concentration-induced quenching of NIR PL. The concentration quenching is attributed to the cross relaxation between the Yb^{3+} ions. It is important to note that though the number of Yb^{3+} ions in the excited state seems to be conserved by the cross relaxation process, however, it is in fact significantly reduced, as the energy migration can cause the excitation not to be deactivated through luminescence, but to be delivered to the quenching sites (traps) within or on the surface of these nanoparticles. A higher Yb^{3+} ion concentration favors energy migration due to a shorter distance between Yb^{3+}ions, and allows the migration of excitation energy to reach trapping sites more readily, consequently resulting in luminescence quenching. To further prove the ET between Tb^{3+} and Yb^{3+}, the excitation spectra were acquired for PL of Tb^{3+} (at 532 nm, $^5D_4 \rightarrow {}^7F_5$ transition) and

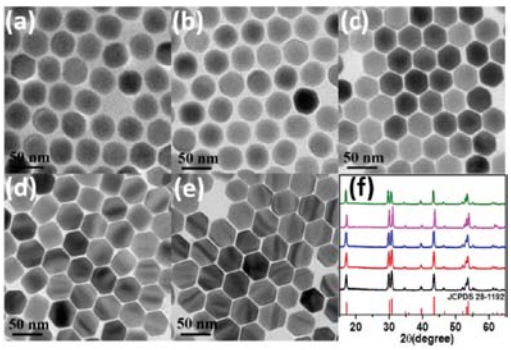

Figure A.6.2. TEM images of $NaYF_4$:2%Tb^{3+} co-doped with (a) 0%, (b) 20%,(c) 40%, (d) 60% and (e) 80% Yb^{3+}, (f) XRD patterns of the synthesized nanoparticles along with the standard pure hexagonal phase of $NaYF_4$ asa reference (JCPDS no. 028-1192).

Yb^{3+} (at 990 nm, $^2F^{5/2} \rightarrow {}^2F^{7/2}$ transition). The coincidence of the PL excitation spectra observed at ~532 nm and at ~990 nm illustrates ET from Tb^{3+} to Yb^{3+} ions. The decays of the VISPL at 542 nm (excited at 355 nm) and of the NIR PL of Yb^{3+} at990 nm (excited at 980 nm) for nanoparticles with different concentrations of Yb^{3+} were also acquired; the observed shortening of the lifetime of PL at ~542 nm with the increase in theYb^{3+} concentration confirms the occurrence of ET between theTb^{3+} and the Yb^{3+} ions. The observed shortening of the Yb^{3+} NIR PL lifetime at ~1000 nm with an increase in the Yb^{3+} ion concentration illustrates the concentration-related quenching of NIR PL due to cross-relaxation between the Yb^{3+} ions. Using the decays for VIS PL, the theoretical QC efficiency can also be determined.

Based on the measured lifetime, the maximal QC efficiency can be as high as ~173% for nanoparticles doped with the Yb^{3+} concentration of 80%. Yet, the NIR PL was found to be the most intense for the sample with the lowest doping concentration of 20%Yb^{3+} (Figure A.6.3a), where the concentration-quenching is the lowest (corresponding to a theoretical QC efficiency of 144.83%). The intensity of NIR PL emission of the sample doped with 20%Yb^{3+} is about 1.2times higher than that of $NaYF_4$:2%Tb^{3+},40%Yb^{3+}, and 2 and7 times higher than that of nanoparticles doped with 40% and 80% Yb^{3+} ions, respectively (Figure A.6.3a). The same behavior for NIR PL from Yb^{3+} was observed when directly exciting the $^5D_4$state of the Tb^{3+} ions at 488 nm (Figure A.6.3b). Since nanoparticles of $NaYF_4$:2%Tb^{3+},20%Yb^{3+} display the most intense NIR PL, these doping concentrations were used in the next experiment.

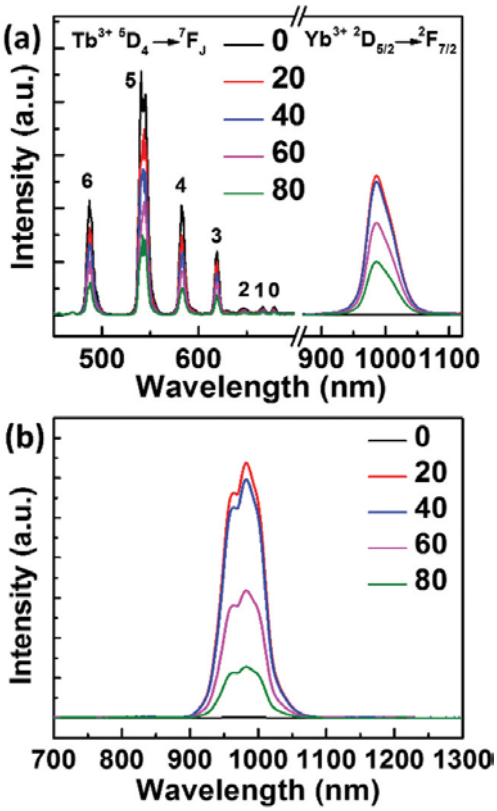

Figure A.6.3. PL spectra of $NaYF_4$ doped with 2%Tb^{3+} and 0, 20, 40, 60, 80%Yb^{3+} excited at (a) 355 nm and (b) 488 nm.

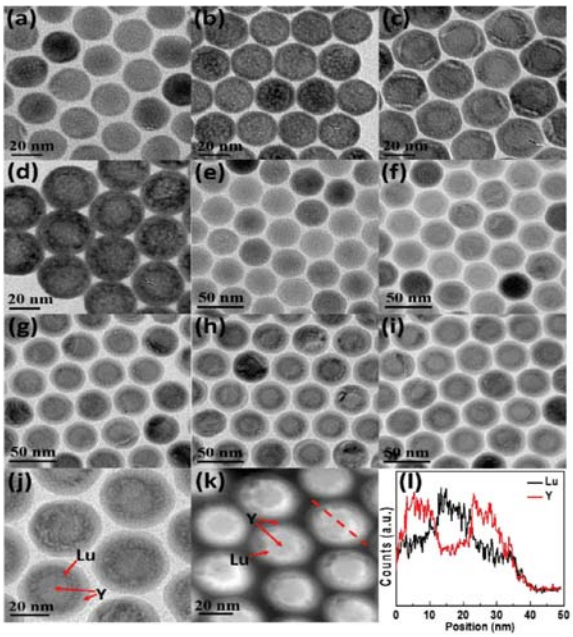

Figure A.6.4. (a–d): Bright field TEM images of $NaYF_4$:10%Er^{3+}@$NaLuF_4$ with$NaLuF_4$ thickness of (a) 1.5 nm, (b) 3 nm, (c) 4 nm, (d) 5 nm. (e–i): $NaYF_4$:10%Er^{3+}@$NaLuF_4$@$NaYF_4$:2%Tb^{3+},20%Yb^{3+}@ $NaYF_4$ with $NaLuF_4$ thickness of(e) 0 nm, (f) 1.5 nm, (g) 3 nm, (h) 4 nm and (i) 5 nm. The (j) bright field TEMimage with higher magnification times, and the (k) dark-field TEM image, ofnanoparticles of $NaYF_4$:10%Er^{3+}@$NaLuF_4$@$NaYF_4$:2%Tb^{3+},20%Yb^{3+}@ $NaYF_4$with a $NaLuF_4$ layer thickness of 5 nm. (l) A line scanning of a single nanoparticleof $NaYF_4$:10%Er^{3+}@$NaLuF_4$@$NaYF_4$:2%Tb^{3+}, 20%Yb^{3+}@$NaYF_4$ with a$NaLuF_4$ layer thickness of 5 nm.

After optimizing the UC and QC emission intensities in regard to dopant concentrations, we combined UC and QC processes together within the same nanoparticles, realizing the core–multishell architecture through an epitaxial growth strategy. We have chosen to have UC in the core domain and QC in the shell domain, since it looks preferable to have the UV-Visible excitable QC process close to the nanoparticle surface than in the core, because of higher scattering for UV light. At the same time, the NIR light used to excite UC PL is not scattered much in this arrangement, which allows us to combine efficient NIR-excitable UC and UV-VIS excitable QC processes within the core–multishell nanostructure. Er^{3+} ions were selected as the dopant to realize the UC process, which have shown efficient UC PL when doped into fluoride nanocrystals under excitation at ~1.5 μm. Thus, the designed core–multishell nanostructure includes the UC core containing Er^{3+}ions, and the active QC shell containing Tb^{3+}/Yb^{3+} ion combination, as discussed above. We employ an inert layer with low phonon energy ($NaLuF_4$) to separate the active core and shell and minimize the detrimental cross-relaxation between active layers separated by this inert layer. $NaLuF_4$ is an excellent host lattice, which enables the $NaYF_4$:10%Er^{3+}@$NaLuF_4$ core/shell nanoparticle to emit with the same efficiency as the $NaYF_4$:10%Er^{3+}@$NaYF_4$ core/shell nanoparticle. Yet, the difference between the atomic numbers of Lu and Y is able to produce a TEM imaging contrast between the $NaLuF_4$ and $NaYF_4$ domains in a single nanoparticle, providing compelling evidence for the formation of a core/multishell nanostructure. The outmost inert shell layer in the $NaYF_4$:10%Er^{3+}@$NaLuF_4$@$NaYF_4$:2%Tb^{3+},20%Yb^{3+}@$NaYF_4$ core–multishell nanoparticles is utilized to suppress surface-related quenching effects. These nanostructures were prepared using a method adapted from our recent work which can reach anatomic monolayer deposition precision. It should be noted that the deposition of an inert $NaYF_4$ layer on the surface of

$NaYF_4$:10%Er^{3+}@$NaLuF_4$@$NaYF_4$:2%Tb^{3+},20%Yb^{3+} resulted in about 3-fold enhancement of QC NIR PL, due to suppression of surface-related quenching. Owing to a high phase contrast between $NaYF_4$ and $NaLuF_4$,the prepared core–multishell nanostructures as well as the involved transition core–shell structures can be clearly resolved by TEM microscopy. The morphology and size distributions of the consecutive nanostructures of NaYF4:10%Er^{3+} (core),$NaYF_4$:10%Er^{3+}@$NaLuF_4$ (core @inert layer), $NaYF_4$:10%Er^{3+}@$NaLuF_4$@$NaYF_4$:2%Tb^{3+},20%Yb^{3+} (core@inert layer@active shell) and $NaYF_4$:10%Er^{3+}@$NaLuF_4$@$NaYF_4$:2%Tb^{3+},20%Yb^{3+}@$NaYF_4$ (core@inert layer@active shell@inert shell) can be determined from the TEM images and size histogram results presented in Figure A.6.4. As can be seen in Figure A.6.4a–e, the periphery of nanoparticles looks darker than the center area, illustrating the formation of $NaLuF_4$ on the surface of $NaYF_4$:10%Er^{3+} nanoparticles and allowing us to evaluate the thickness of the $NaLuF_4$ layer. Moreover, the formation of $NaYF_4$:2%Tb^{3+},20%Yb^{3+} and $NaYF_4$ layers on$NaYF_4$:10%Er^{3+}@$NaLuF_4$ nanoparticles can be confirmed by TEM (Figure A.6.4f–j) and linear scanning of a single nanoparticle inthe dark-field TEM image (Figure A.6.4k and l), which is consistent with the recent report that elements can be confined in the core–shell by a solution synthesized method. Thus, the TEM results substantiate the formation of NaYF4:10%Er^{3+}@$NaLuF_4$@$NaYF_4$:2%Tb^{3+},20%Yb^{3+}@$NaYF_4$ core–multishell nanostructures with varying thicknesses of the first inert layer.

We excited the core–multishell nanoparticles of $NaYF_4$:10%Er^{3+}@$NaLuF_4$@NaYF4:2%Tb^{3+},20%Yb^{3+}@$NaYF_4$ at 1523 nm (18W cm^{-2}) and 488 nm (0.45 W cm^{-2}), respectively (according to the absorption spectrum of $NaYF_4$:10%Er^{3+}@$NaLuF_4$@$NaYF_4$:2%Tb^{3+},20%Yb

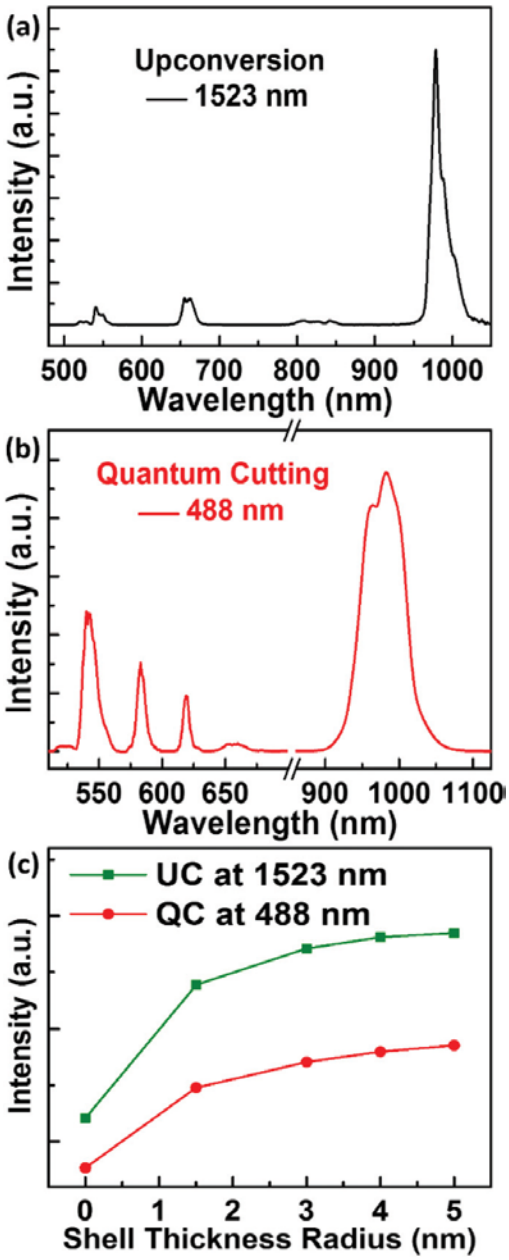

Figure A.6.5. PL spectrum of $NaYF_4$:10%Er^{3+}@$NaLuF_4$@$NaYF_4$:2%Tb^{3+},20 %Yb^{3+}@$NaYF_4$ nanoparticles excited at (a) 1523 nm (18 W cm^{-2}) and(b) 488 nm (0.45 W cm^{-2}). (c) The dependencies of integrated UC PL and QC PL intensities on the thickness of the NaLuF4 inert layer in the core–multishell nanoparticles of $NaYF_4$:10%Er^{3+}@$NaLuF_4$@ $NaYF_4$:2%Tb^{3+},20%Yb^{3+}@$NaYF_4$.

$^{3+}$@$NaYF_4$ nanoparticles). The obtained spectra in Figure A.6.5a and b show the UC emission from Er^{3+} and the QC emission from Yb^{3+}/Tb^{3+}, revealing that both UC and QC processes can work independently in the designed core–multishell structure. Note that, despite the existence of the PL peak at~980 nm from Er^{3+} ions when excited at 488 nm, the observed NIR PL peak at ~980 nm in Figure A.6.5b mainly arises from the QC process of the Tb^{3+}/Yb^{3+} ion pairs, as indicated by the comparison of PL spectra from $NaYF_4$:10%Er^{3+}@$NaLuF_4$ and $NaYF_4$:10%Er^{3+}@$NaLuF_4$@$NaYF_4$:2%Tb^{3+},20%Yb^{3+}@$NaYF_4$ nanoparticles. The integrated PL intensities of UC and QC were plotted versus the thickness of the first isolation layer of $NaLuF_4$ (Figure A.6.5c). As one can see, both the UC and QC PL intensities increase with an increase in the thickness of the $NaLuF_4$ layer from 0 (no inert layer) to 1.5 nm, reaching an apparent plateau of1.7-fold enhancement when the thickness is over 3 nm. This observation verifies that the inert shell $NaLuF_4$ layer can reduce detrimental cross-relaxation processes between the UC core and the QC shell, and such a quenching effect can be eliminated when the thickness is beyond a threshold value of 3 nm. The intensity of NIR QC PL from the core/multishell $NaYF_4$:10%Er^{3+}@$NaLuF_4$@$NaYF_4$:2%Tb^{3+},20%Yb^{3+}@$NaYF_4$ nanoparticles is almost identical to that from the core/shell NaYF4:2%Tb^{3+},20%Yb^{3+}@$NaYF_4$ nanoparticles with an inert shell thickness of ~4.2 nm, indicating a negligible surface-related quenching effect of the core/multishell nanostructure. The luminescence quantum yield is an important parameter to characterize the radiative ability of photoluminescent materials; it is defined by the ratio of the number of emitted luminescent photons to the number of the absorbed excitation photons. For the core/multishell $NaYF_4$:10%Er^{3+}@$NaLuF_4$@$NaYF_4$: 2%Tb^{3+},20%Yb^{3+}@$NaYF_4$ colloidal nanoparticles, we found the upconversion quantum yield to be~ 1.6%, and the luminescence yield of the quantum cutting process was found to be as high as ~130%. The realization of over-a-unit luminescence quantum yield of a QC process in colloidal core/multishell nanocrystals holds promises for a

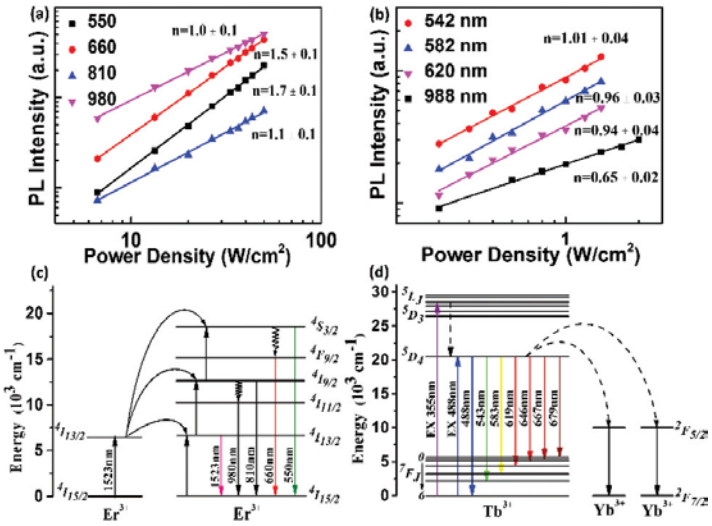

Figure A.6.6. Dependencies of emission intensities on excitation power density for (a) UC PL excited at 1523 nm and (b) QC PL excited at488 nm. (c) Energy diagram illustrating the mechanism of Er^{3+} UC process. (d) Energy diagram illustrating the mechanism of Yb^{3+}–Tb^{3+}QC process.

plethora of photonic applications as described earlier.

To establish the mechanisms of the UC and QC processes simultaneously occurring in the core–multishell nanoparticles, the dependence of the PL intensity on the excitation power density was investigated for the core–multishell nanoparticles with a 3 nm inert layer. The number of photons involving in both the UC and QC processes can be calculated based on the formula: $I \propto P^n$, where I is the PL emission intensity, P is the pump laser power density, and n is the number of photons involved in the excitation process. As shown in Figure A.6.6a, the power density dependencies for the four UC PL bands plotted in a log–log scale are nearly linear. The slopes of the fitting lines, were 1.73 ± 0.01, 1.53 ± 0.03, 1.11 ± 0.02 and 1.02 ± 0.01,for the emissions at 550, 660, 810, and 980 nm respectively, which are similar to those in our previous reports, yet different from the actual number of photons involved for the 980 (2-photon), 810 (2-photon), 660 (3-photon), and 550 nm(3-photon) UC emissions. The deviation of our results from the real numbers of photon processes is associated with the saturation effect in the intermediate $^4I_{13/2}$ state, which has a long lifetime to produce a reservoir for excited populations. On the other hand, the slope for dependencies of QC PL emission peaks at 542, 582, 620, and 990 nm, which correspond to $^5D_4 \rightarrow {}^7F_5$, $^5D_4 \rightarrow {}^7F_4$, $^5D_4 \rightarrow {}^7F_3$, and $^2F_{5/2} \rightarrow {}^2F_{7/2}$ transitions, were determined to be 1.01 ± 0.04, 0.96 ± 0.03, 0.94 ± 0.04, and0.65 ± 0.02, respectively (Figure A.6.6b). The sublinear dependence of NIR PL on the excitation power density at ~990 nm clearly demonstrates the occurrence of a quantum cutting process, i.e. the ET process from one single Tb^{3+} ion to two Yb^{3+} ions. The mechanisms illustrating both UC and QC processes are schematically illustrated in Figure A.6.6c and d.

A.7. ICG-Sensitized $NaYF_4$:Er Nanostructure for Theranostics

In this work, addressing the problem of low absorption of Er^{3+}-doped LNPs, we report the design and synthesis of indo-cyanine green (ICG) dye sensitized $NaYF_4$:Er LNPs. ICG has strong absorption at 808 nm with large Stokes-shifted emission band that overlaps with the Er^{3+} absorption band (Scheme A.7.1), enabling efficient energy transfer from ICG to Er^{3+}ions. We developed sensitizing of $NaYF_4$:Er LNPs by the ICG dye resulted in improvement of Er^{3+} doping concentration from2 to 20 mol%. Both the upconverted32(-fold) and Stokes(≈5-fold) emissions (1520 nm) in NIR-II window of LNPs were enhanced. Efficient

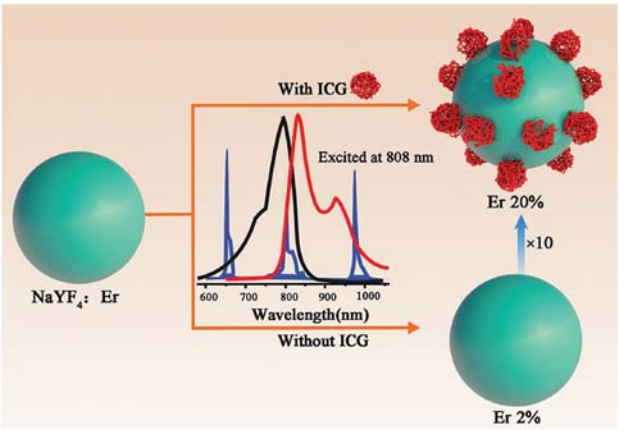

Scheme A.7.1. Schematic illustration of the optimal Er^{3+}doping concentration with and without ICG sensitization. The overlap between emission of ICG and absorbance of Er^{3+}-doped LNPs was shown in center.

energy transfer from the ICG molecules also reduces photobleaching of the dye and provides better photostability of this conjugate for bioimaging applications. To show the potential of the designed nanoconstruct in bioapplications, we used ICG-$NaYF_4$:Er for bioimaging in three modalities simultaneously. The Stokes emission of Er^{3+} ions centered at≈1.5 μm provided imaging mode in NIR-II optical transparency window. On the other hand, ICG as an efficient photoacoustic contrast agent, approved by the Food and Drug Administration, was also used in our current work for photoacoustic imaging (PAI) enabled by local heating that is produced due to the competing nonradiative process. The capability of ICG to generate heat and raise the local temperature under optical excitation provides opportunity for photothermal imaging (PTI) and photothermal therapy. All the three imaging modalities including PTI, PA, and NIR-II imaging, discussed in this study, represent high potential for emerging theranostics technologies. The major strength of the nanoconstruct presented here is that it has the capability to be used as a probe for multiplex imaging integrating all these modalities.

Synthesized $NaYF_4$:Er LNPs for all set of Er^{3+} concentrations between 2 and 100 mol% had a uniform size (Figure A.7.1a). The crystallographic phase and the stoichiometric composition of LNPs were demonstrated, demonstrating hexagonal crystallographic phase. A gradual increase of peak intensities for the Er^{3+} element manifests the rational design and successful doping of Er^{3+} in LNPs. When excited at 808 nm, the$NaYF_4$:Er LNPs emits at 540 nm, 650 nm in the visible (upconverted emission) and1520 nm (Stokes emission) in the NIR range. The power dependences of the 540, 650, and1520 nm emissions showed classical quadratic functions for the upconverted emissions with slopes of 1.89 and 1.95 for 540 and650 nm, respectively, and linear dependence for the Stokes emission centered at 1520 nm.

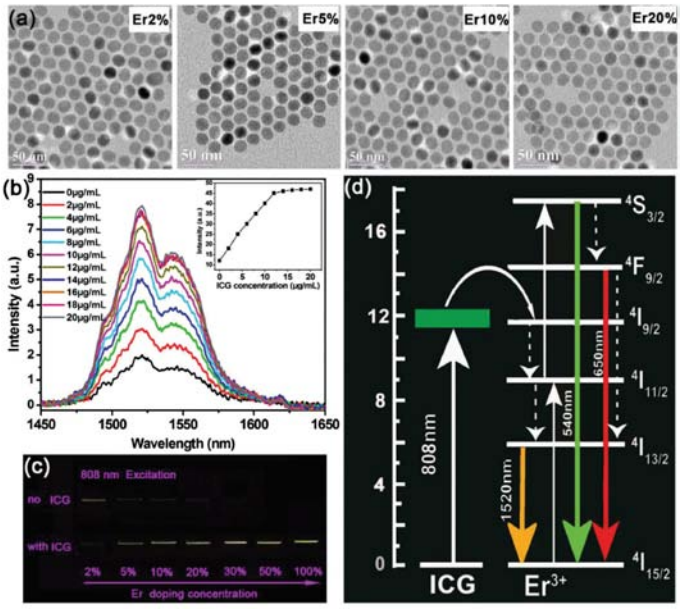

Figure A.7.1. a) TEM images of the $NaYF_4$:Er nanocrystals at Er^{3+}doping levels from 2 to 20 mol%. b) Stokes emission centered at 1520 nm of the $NaYF_4$:Er (20%) LNPs with different concentration of ICG sensitized under 808 nm excitation. Inset shows integrated intensity as a function of ICG concentration. c) The luminescence photographs of $NaYF_4$:Er LNPs under 808 nm excitation (0.67 W cm^{-2}). d) Proposed upconversion mechanism of ICG-sensitized Er^{3+}doped LNPs.

To enhance the brightness of LNPs emission, we first optimized the concentration of ICG in the ICG-LNPs conjugate. For conjugation, the oleic acid ligand on the surface of the LNPs was first substituted with nitrosonium tetrafluoroborate ($NOBF_4$). Ligand exchange did not produce any significant luminescence quenching.

Then ICG was added and attached to the LNPs surface through the sulfonic acid group, as we reported previously. We found that the luminescence intensity of$NaYF_4$:Er (20%) LNPs was significantly improved with an increase in the amount of the ICG dye in solution, reaching a maximum at the ICG concentration of 14 μg mL^{-1} (Figure A.7.1b).From Figure A.7.1c, greatly visible upconverted emission can be observed from $NaYF_4$:Er LNPs upon 808 nm laser irradiation. The energy level diagram and the possible transitions between ICG and LNPs are shown in Figure A.7.1d. The luminescence intensity from $^4I_{9/2}$, states increases first with the increased surface binding of ICG dye, which is consistent with increasing overall absorption of the excitation energy at 808 nm. However, the luminescence decreased when ICG concentration reached beyond a certain value, which is ascribed to the selfquenching effect between the ICG molecules on the LNPs surface, and an increasing concentration of unanchored ICG molecules absorbing the 808 nm illumination, which results in screening of the ICG-LNPs conjugate. The estimated number of ICG dye molecules on per LNP by protocol was ≈21. The optimum concentration of ICG(14 μg mL−1) resulted in 1.2-, 2.17-, 4.93-, 5.41-, 3.93-, 2.85-, and 2.32-fold enhancement of Stokes emission for different level of Er^{3+} doping LNPs (Figure A.7.2a,b). After ICG sensitization, the optimum Er^{3+} concentration was shifted from 2 to 20 mol% for LNPs. The efficiency of energy transfer from ICG to the LNPs was estimated to be≈45%, and the luminescence quantum yield was measured using protocol described to be ≈3.1%.

We further compared the Stokes emission intensity of ICG$NaYF_4$:Er LNPs pumped by 808 nm with that of the $NaYF_4$:Yb/Er (20/2%) LNPs pumped by 980 nm laser. In both cases the concentration of nanoparticles and the power density of both pump laser beams lasers were the same. The intensity of the 1520 nm emission from the ICG sensitized LNPs was≈10 times higher than that for the Yb/Er co-doped system.

Upconverted emission is also enhanced by ICG sensitizing. Because of concentration quenching effect, this emission for pure $NaYF_4$:Er LNPs decreased by increasing the Er^{3+} concentration, resulting in maximum integrated emission intensity (510–675 nm) at 2 mol% of the Er^{3+} concentration. Both visible luminescence bands are completely

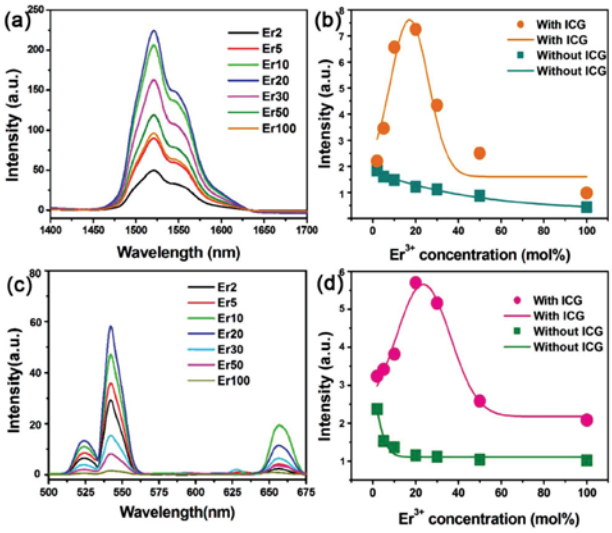

Figure A.7.2. a) Stokes emission spectrum centered at 1520 nm of the $NaYF_4$: Er (*x*%) (*x* = 2, 5, 10, 20, 30, 50, 100) LNPs (≈5 mg mL^{-1}, DMF) with optimum ICG concentration (14 μg mL^{-1}) sensitized under 808 nm excitation. b) Integrated intensity centered at 1520 nm of LNPs as a function of Er3+ concentration. c) Upconversion emission spectra between 500 and 675 nm of the $NaYF_4$:Er (*x*%) (*x* = 2, 5, 10, 20, 30, 50, 100). d) Integrated intensity visible emission from510 to 675 nm as a function of Er^{3+}concentration.

quenched at 100% of the Er^{3+} ion concentration. When sensitized by ICG, the visible emission reached maximum intensity at 20% of Er^{3+} ion concentration, and was≈32 times stronger compared to that of the nonsensitized LNPs (Figure A.7.2c,d). For optimal concentrations of Er^{3+} ions (20%) and ICG dye (14 μg mL−1),the ICG sensitized LNPs under 808 nm excitation yielded ≈40%higher upconverted emission intensity compared to that of$NaYF_4$:Yb/Er (20/2%) LNPs under 980 nm with the same power density. Actually, this elevation of Er^{3+} doping concentration is reasonable. Because doping low Er3+ concentration will result in few Er^{3+} ions on surface, which is un-benefit for ICG-sensitization. On contrast, doping high Er^{3+} concentration will lead to large amounts of Er^{3+} ions on surface, which generates many channels to fulfill ICG-sensitization.

For biomedical applications capability, we modified the nanomaterial to make it dispersible in water by conjugating DSPE-mPEG. The size of the DSPE-mPEG/ICG-LNPs nanoconstruct, estimated by the dynamic light scattering technique, was found to be 130.3 ± 2.1 nm. The quantum yield was measured to be ≈1.9% after transferred to aqueous solution. To evaluate the cytotoxicity of DSPE-mPEG/ICG-LNPs, we measured the cell viability with the MTT assay based on 3-(4,5-dimethyl-2-thiazolyl)-2, 5-diphenyl-2-H-tetrazolium bromide. For Hela cells used for the cytotoxicity experiment, showed 85% survivability at the concentration of 1 mg mL^{-1} after 48 hours of incubation with DSPE-mPEG/ICG-LNPs, and almost 90% rat C6 glioma cells were survived after treatment using 1 mg mL^{-1} DSPE-mPEG/ICGLNPs dispersion, supporting the good biocompatibility feature of nanoconstructs. Monitoring of the intensity of Stokes emission at 1520 nm of DSPE-mPEG/ICG-LNPs dispersed in water (2 mL, 1 mg mL^{-1}) detected only a twofold decrease in the intensity after 6 h, demonstrating relative stability of dye component in the conjugate.

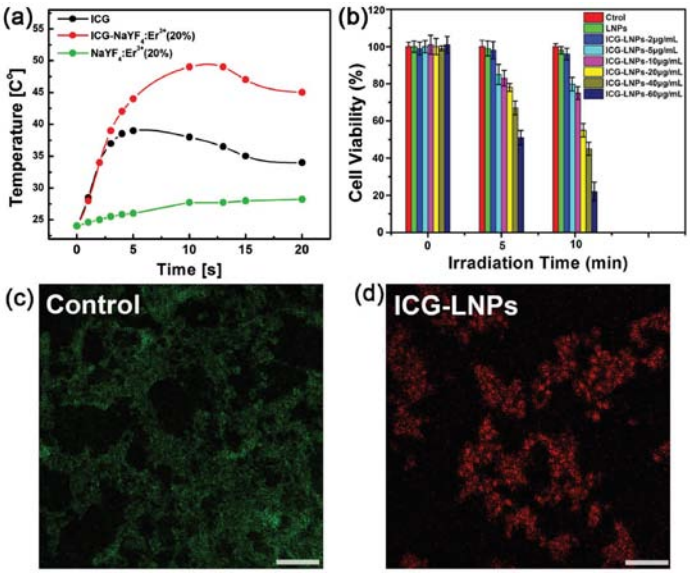

Figure A.7.3. a) Temperature increase induced by optical (808 nm) excitation corresponds to ICG-NaYF4:Er (20%) solution in DMF (red), pure ICG solutions in DMF (black), pure NaYF4:Er (20%) LNPs (green). b) MTT assay results. c,d) Efficiency of the photothermal destruction of rat C6 cells evaluated by staining with calcein and PI in green and red spectral channels, correspondingly.

To validate our nanoconstructs for bioimaging, potential side effects of DSPE-mPEG/ICG-LNPs were evaluated. In these experiments, healthy BALB/c mice were intravenously injected with DSPE-mPEG/ICG-LNPs through the tail vein. After 15 d, the blood was collected and the standard hematology parameters including white blood cells,

red blood cells, hemoglobin, hematocrit, mean corpuscular hemoglobin, mean corpuscular hemoglobin concentration, platelets, and mean corpuscular volume were measured. We also tested the blood biochemical indices including alanine transaminase, aspartate transaminase, total protein, globulin, total bilirubin, blood urea nitrogen, creatinine, and albumin. The above results indicate that the DSPE-mPEG/ICG-LNPs did not cause inflammation and infection in the treated mice.

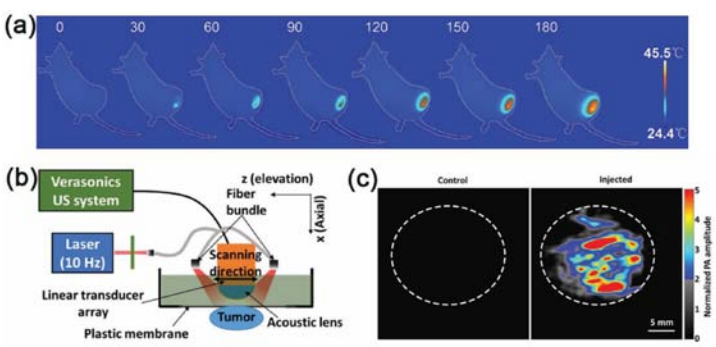

Figure A.7.4. a) PTI of nude mice, thermal gradient area corresponds to pancreatic tumor site irradiated by an 808 nm laser for 0, 30, 60, 90, 120, 150,and 180 s. b) Schematic drawing for PAI arrangement. c) PAI of the same tumor as for PTI and NIR-II. Both, PTI and PAI images were captured from the same pancreatic tumor at the same injection of DSPE-mPEG-2000/ICG LNPs.

In addition, histological analysis showed no inflammatory response, nor any tissue injury in the DSPE-mPEG/ICG-LNPs-treated mice, as compared to the control group. All these results indicate sufficient biocompatibility of DSPE-mPEG/ICG-LNPs.

It has been previously demonstrated that ICG absorbs NIR light at 808 nm and emits the energy as heat, making it a valuable agent for localized hyperthermia with a rapid rate of temperature increase. At the same time, NaYF4:Er LNPs may act as nanoheaters by itself. To investigate the role of these two components(ICG and LNPs itself) in the localized heating process under optical excitation, we studied the dynamics of thermal heating induced by the pure ICG component, LNPs and the ICG-LNPs nanoconstructs. The results of this study (Figure A.7.3a) demonstrate that in cases of ICG and ICG-LNPs conjugate the initial rise of temperature up to ≈2 s occurred at same rate. However, with continuing irradiation we observed a significant difference between the photothermal response of ICG and ICG-LNPs. In experiments with pure ICG, the local temperature reached maximum of ≈40° C following ≈5 s of irradiation. In contrast, the ICG-LNPs nanoconstructs continued to increase local temperature until it reached ≈50 ° C at ≈12 s of irradiation (Figure A.7.3a). At the same time, pure LNPs demonstrated small (≈2.5 ° C) increasing of the temperature, which manifests insignificant role of LNPs as nanoheaters in comparison to ICG-LNPs conjugate. The decreasing temperature gradient in ICG and ICG-LNPs is most likely due to bleaching of the dye. In the case of ICG-LNPs nanoconstructs, an efficient energy transfer from ICG to Er^{3+} ions prevents over-excitation and intensive bleaching of ICG and, therefore, supplies favorable conditions for localized thermal heating.

To investigate the photothermal effect of DSPE-mPEG/ICG-LNPs in vitro, these nanoconstructs at final concentrations ranging from 2 to 60 μg mL^{-1}, were incubated with and

incorporated into rat C6 cells. Then, cells were washed to remove free nanoconstructs, and irradiated with 808 nm light for either 5 or 10 min, and subjected to the MTT assay. These experiments show a high photothermal effect of our nanoconstructs, wherein the cytotoxicity was strictly dependent on the concentration of nanoconstructs and the irradiation dose. The nanoconstructs, at the lowest tested concentration of 2 μg mL^{-1}, produce no visible changes in the cellular viability, regardless of the irradiation time. At the concentration of 5 μg mL^{-1}, we observed a ≈15% and ≈20% drop in the cellular viability, following the 5 and 10 min irradiation treatment, respectively. At 60 μg mL^{-1}, our nanoconstructs produce a ≈50% drop in the cellular viability following 5 min irradiation, and ≈80% drop following 10 min irradiation (Figure A.7.3b). In the absence of irradiation (control), no changes in the cellular cytotoxicity were found, regardless of the concentration of nanoconstructs (Figure A.7.3b).

In parallel, we characterized the photothermal effect of our nanoconstructs using optical imaging. In these experiments, cells following the incubation with highest concentration of nanoconstructs, as well as nanoconstructs free-cells for control, were irradiated for 10 min and stained with calcein AM and propidium iodide (PI). In this assay, calcein is selectively accumulated in the metabolically active, undamaged cells, while PI stains genomic DNA of necrotic cells. In the control cells, which were not incubated with nanoconstructs, calcein staining was intense and no signal from PI was observed, which is consistent with MTT results. In contrast, the cells, which incorporated the nanoconstructs, demonstrated extensive photothermal damage. We found that PI stained virtually every cell in the dish, while the signal of calcein was absent (Figure A.7.3c,d). These results convincingly demonstrate high potential of the DSPE-mPEG/ICG-LNPs nanoconstructs as an efficient agent for photothermal therapy.

Next, we explored our nanoconstructs for photothermal imaging in vivo. Figure A.7.4a shows thermal images of the mouse tumor before (control) and after injection. According to the temperature coding bar, the surface temperature of the irradiated tumor site has changed from ≈24 °C before injection up to 45 °C after 180 s of irradiation of the injected area. To estimate the temperature at the depth of nanoconstruct localization, we studied the dissipation of thermal heating through the depth of a chicken breast tissue from the point-like steady heating source. For this experiment, we used fresh cut slices of chicken breast, which were heated by point-like black metallic target irradiated by the focused laser beam from one side, and imaged by the thermal camera from the other side. Using the result of this experiment, we estimated the temperature generated by the nanoconstructs within the tumor site at the depth ≈2 mm as ≈ 61° C, which is enough to produce photothermal therapy to destroy the tumorous tissue. This estimation indicates that our nanoconstruct, ICG-LNPs, can be used as an efficient agent for photothermal therapy.

Next, we explored the utility of ICG-LNPs for PAI of murine tumors using a pulsed-laser PAI system (Figure A.7.4b). Tumors were imaged in mice with or without intratumor

administration of ICG-LNPs. Figure A.7.4c shows the maximum amplitude projection PA image of the control and administrated tumors. Because the intrinsic optical absorption of the control tumor is low, its PA signal was weak and was shown completely in dark gray according to the color-coded signal intensity scale (Figure A.7.4c). However, for the one injected with ICG-LNPs, intense PA signals were observed in the tumor region, as indicated by the color scale. We could observe a gradient in distribution of ICGLNPs using PAI modality. Inherent to the intratumor injection distribution of LNPs was nonuniform. Analysis of signal intensities indicates that the PA signal intensity in injected tumor is ≈5 times higher than that of control, indicating that ICG-LNPs produce a high contrast for PAI modality.

To verify the capability of ICG-$NaYF_4$: Er LNPs imaging properties in the NIR-II optical window at 1520 nm, we studied transmission for three types of biological tissue samples using Stokes emission from LNPs. The arrangement of the experiment was the following. The LNPs solution sample with the optimal concentrations of ICG and Er^{3+} ions was sealed in a capillary tube (ø 300μm, 10 mm) to mimic an emitting source(Figure A.7.5a). The sample was irradiated by 808 nm laser diode to produce fluorescence NIR signal. Then tissue slices of different thickness were inserted between the illuminated LNPs sample and imaging camera and the transmitted NIR light through the tissue slices was imaged (Figure A.7.5b,d). The results of the experiment demonstrated the capability of using ICG-$NaYF_4$:ErLNPs for optical NIR-II imaging through the biological tissue at depths up to 1.5–2.5 mm, depending on the type of tissue(Figure A.7.5e).

The capability of application of ICG-LNPs for imaging in the NIR-II optical window was further demonstrated by the example of the pancreas tumor site imaging of an intact nude mouse. As expected, we could not detect any signal at 1520 nm, without the injection of DSPE-mPEG/ICG-LNPs nanoconstructs (Figure A.7.5f). However, after injection of our nanoconstructs(1 mg mL^{-1}, 200 μL), we observed intense signal around 1520 nm, which come from Er^{3+} emission of

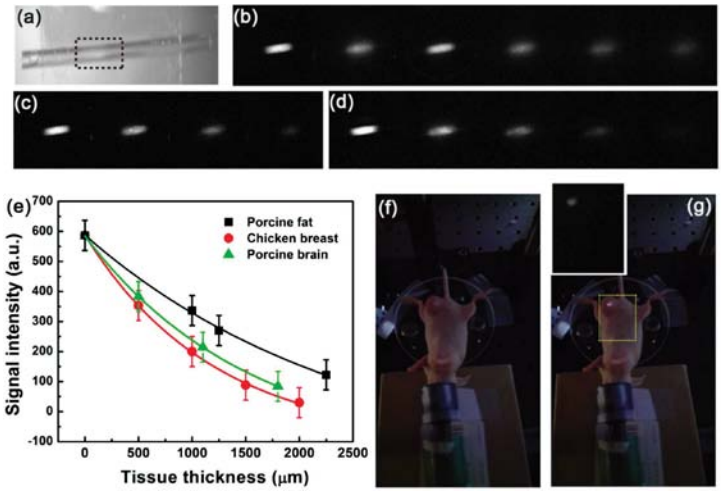

Figure A.7.5. a) Capillary tube (ø 300 μm, 10 mm) with ICG-LNPs inside used for NIR emission transmission, b–d) images of ICG-LNPs NIR emissioncentered at 1520 nm through the porcine fat (b), chicken breast (c), and porcine brain (d) tissue slices of different thickness. e) Transmission ofStokes emission at 1520 nm of ICG-$NaYF_4$:Er(20%) LNPs (aqueous phase) through different biotissue slices. f,g) NIR-II in vivo optical imaging ofDSPE-mPEG-2000/ICG LNPs injected in tumor. f) Bright field of pancreas tumor-bearing mouse, dark field image at NIR-II (≈1520 nm) of tumor area.g) An overlap of bright field and NIR images.

DSPE-mPEG/ICG-LNPs. The inset picture in Figure A.7.5g showed the dark field imaging after injection of nanoconstruct. The images were obtained from (≈2 mm) skin layers. The results demonstrated that DSPE-mPEG/ICG-LNPs seem to be an excellent candidate and attractive infrared nanoprobes for in vivo imaging in the NIR-II window.

B. Related Publications during Reporting Period:

1. Guanying Chen, Wei Shao, Rashid R. Valiev, Tymish Y. Ohulchanskyy, Guang S. He, Hans Ågren, and Paras N. Prasad. Efficient Broadband Upconversion of Near-Infrared Light in Dye-Sensitized Core/Shell Nanocrystals. *Adv. Optical Mater.* 2016, 4, 1760-1766.

2. Wei Wei, Guanying Chen, Alexander Baev, Guang S. He, Wei Shao, Jossana Damasco, and Paras N. Prasad. Alleviating Luminescence Concentration Quenching in Upconversion Nanoparticles through Organic Dye Sensitization. *J. Am. Chem. Soc.* 2016, 138, 15130-15133.

3. Wei Shao, Guanying Chen, Andrey Kuzmin, Hilliard L. Kutscher, Artem Pliss, Tymish Y. Ohulchanskyy, and Paras N. Prasad. Tunable Narrow Band Emissions from Dye-Sensitized Core/Shell/ Shell Nanocrystals in the Second Near-Infrared Biological Window. *J. Am. Chem. Soc.* 2016, 138, 16192-16195.

4. Bobo Gu, Artem Pliss, Andrey N Kuzmin, Alexander Baev, Tymish Y Ohulchanskyy, Jossana A Damasco, Ken-Tye Yong, Shuangchun Wen, Paras N Prasad. In-situ second harmonic generation by cancer cell targeting ZnO nanocrystals to effect photodynamic action in subcellular space. *Biomaterials,* 2016, 104, 78-86.

5. Wei Shao, Guanying Chen, Tymish Y. Ohulchanskyy, Chunhui Yang, Hans Ågren and Paras N. Prasad. A core–multiple shell nanostructure enabling concurrent upconversion and quantum cutting for photon management. *Nanoscale*, 2017, 9, 1934-1941.

6. Artem Pliss, Tymish Y. Ohulchanskyy, Guanying Chen, Jossana Damasco, Caroline E. Bass, and Paras N. Prasad. Subcellular Optogenetics Enacted by Targeted Nanotransformers of Near-Infrared Light. *ACS Photonics*, 2017, 4 (4), 806-814.

7. Liang Qiao, Zheng Fu, Ji Li, John Ghosen, Ming Zeng, John Stebbins, Paras N. Prasad, and Mark T. Swihart. Standardizing Size- and Shape-Controlled Synthesis of Monodisperse Magnetite (Fe_3O_4) Nanocrystals by Identifying and ExploitingEffects of Organic Impurities. *ACS Nano*, 2017, 11, 6370-6381.

8. Shuwei Hao, Guanying Chen, Chunhui Yang, Wei Shao, Wei Wei, Yang Liu, and Paras N. Prasad. Nd^{3+}-Sensitized multicolor upconversion luminescence from a sandwiched core/shell/shellnanostructure. *Nanoscale*, 2017, 9, 10633-10638.

9. Depeng Wang, Wei Wei, Ajay Singh, Guang S He, Ramamurthi Kannan, Loon-Seng Tan, Guanying Chen, Paras N Prasad, Jun Xia. Nonlinear Photoacoustic Imaging by in Situ Multiphoton Upconversion and Energy Transfer. *ACS Photonics*, 2017, 4, 2699-2705.

10. Wei Shao, Chang-Keun Lim, Qi Li, Mark T. Swihart, and Paras N. Prasad. Dramatic Enhancement of Quantum Cutting in Lanthanide-Doped Nanocrystals Photosensitized with an Aggregation-Induced Enhanced Emission Dye. *Nano Letters*, 2018, 18, 4922-4926.

11. Chang‐Keun Lim, Anton A Popov, Gleb Tselikov, Jeongyun Heo, Artem Pliss, Sehoon Kim, Andrei V Kabashin, Paras N Prasad. Organic Solvent and Surfactant Free Fluorescent Organic Nanoparticles by Laser Ablation of Aggregation-Induced Enhanced Emission Dyes. *Advanced Optical Materials*, 2018, 6, 1800164.

12. Dan Wang, Depeng Wang, Andrey Kuzmin, Artem Pliss, Wei Shao, Jun Xia, Junle Qu, and Paras N. Prasad. ICG-Sensitized $NaYF_4$:Er Nanostructure for Theranostics. *Adv. Optical Mater.* 2018, 6, 1701142.

13. Ruichan Lv, Miao Feng, Liyang Xiao, Jossana A Damasco, Jie Tian, Paras N Prasad. Multilevel Nanoarchitecture Exhibiting Biosensing for Cancer Diagnostics by Dual-Modal Switching of Optical and Magnetic Resonance Signals. *ACS Applied Bio Materials*, 2018, 1, 1505-1511.